Article

Cell Reports

PML at Mitochondria-Associated Membranes Is Critical for the Repression of Autophagy and Cancer Development

Graphical Abstract

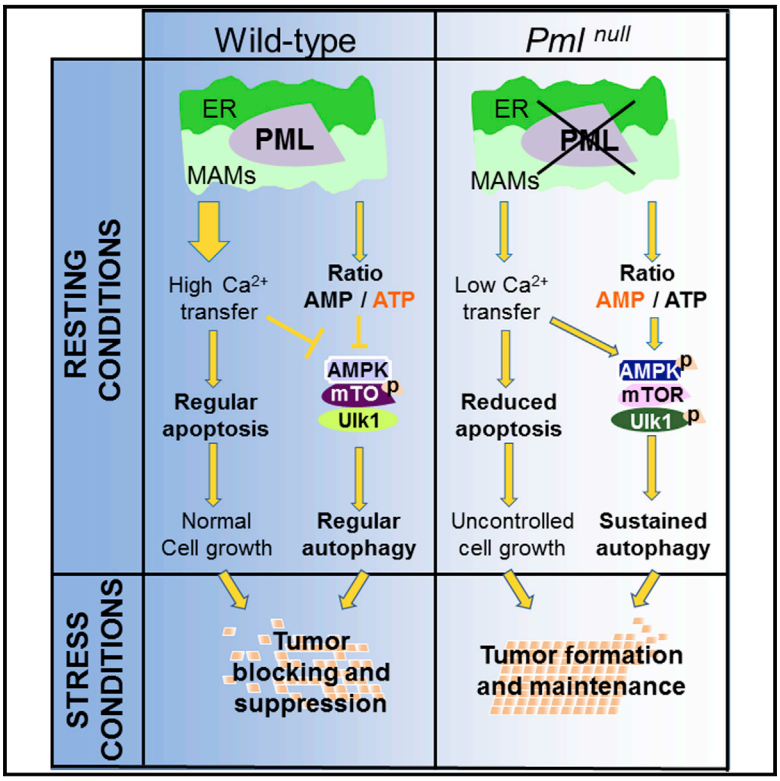

Highlights

- PML regulates autophagic processes from ER/MAM domains in a Ca^{2+}-dependent manner
- Localization of PML away from the MAMs is dependent on p53
- Activation of autophagy by PML depletion promotes survival under stress conditions
- Block of autophagy restores the activity of chemotherapy in PML-downregulated tumors

Authors

Sonia Missiroli, Massimo Bonora, Simone Patergnani, ..., Pier Paolo Pandolfi, Paolo Pinton, Carlotta Giorgi

Correspondence

grgclt@unife.it

In Brief

Missiroli et al. demonstrate that the tumor suppressor promyelocytic leukemia protein (PML) works as a repressor of autophagy by controlling autophagosome formation at mitochondria-associated membranes (MAMs) in a p53-dependent manner. Together, their studies generate alternative anticancer strategies for tumors that present PML downregulation.

Missiroli et al., 2016, Cell Reports *16*, 2415–2427
August 30, 2016
http://dx.doi.org/10.1016/j.celrep.2016.07.082

CellPress

Cell Reports
Article

PML at Mitochondria-Associated Membranes Is Critical for the Repression of Autophagy and Cancer Development

Sonia Missiroli,[1,14] Massimo Bonora,[1,14] Simone Patergnani,[1,14] Federica Poletti,[1] Mariasole Perrone,[1] Roberta Gafà,[2] Eros Magri,[2] Andrea Raimondi,[3] Giovanni Lanza,[2] Carlo Tacchetti,[3,4] Guido Kroemer,[5,6,7,8,9,10,11] Pier Paolo Pandolfi,[12,13] Paolo Pinton,[1] and Carlotta Giorgi[1,15,*]

[1]Department of Morphology, Surgery and Experimental Medicine, Section of Pathology, Oncology and Experimental Biology and LTTA Center, University of Ferrara, Ferrara 44121, Italy
[2]Department of Morphology, Surgery and Experimental Medicine, Section of Anatomic Pathology and Molecular Diagnostics, University of Ferrara, Ferrara 44121, Italy
[3]Experimental Imaging Center, San Raffaele Scientific Institute, Milan 20132, Italy
[4]Department of Experimental Medicine, University of Genoa, Genoa 16132, Italy
[5]Equipe 11 Labellisée par la Ligue contre le Cancer, Centre de Recherche des Cordeliers, Paris 75006, France
[6]Cell Biology and Metabolomics platforms, Gustave Roussy Comprehensive Cancer Center, Villejuif 94800, France
[7]INSERM, U1138, Paris 75006, France
[8]Université Paris Descartes, Sorbonne Paris Cité, Paris 75006, France
[9]Université Pierre et Marie Curie, Paris VI, Paris 75006, France
[10]Pôle de Biologie, Hôpital Européen Georges Pompidou, AP-HP, Paris 75015, France
[11]Karolinska Institute and Department of Women's and Children's Health, Karolinska University Hospital Q2:07, 17176 Stockholm, Sweden
[12]Cancer Genetics Program, Beth Israel Deaconess Cancer Center, Harvard Medical School, Boston, MA 02215, USA
[13]Departments of Medicine and Pathology, Beth Israel Deaconess Medical Center, Harvard Medical School, Boston, MA 02215, USA
[14]Co-first author
[15]Lead Contact
*Correspondence: grgclt@unife.it
http://dx.doi.org/10.1016/j.celrep.2016.07.082

SUMMARY

The precise molecular mechanisms that coordinate apoptosis and autophagy in cancer remain to be determined. Here, we provide evidence that the tumor suppressor promyelocytic leukemia protein (PML) controls autophagosome formation at mitochondria-associated membranes (MAMs) and, thus, autophagy induction. Our in vitro and in vivo results demonstrate how PML functions as a repressor of autophagy. PML loss promotes tumor development, providing a growth advantage to tumor cells that use autophagy as a cell survival strategy during stress conditions. These findings demonstrate that autophagy inhibition could be paired with a chemotherapeutic agent to develop anticancer strategies for tumors that present PML downregulation.

INTRODUCTION

To become cancerous, cells must overcome the foolproof mechanism of cell death, thereby reducing their propensity to activate self-destructive catabolic pathways in response to hostile environmental clues (Hanahan and Weinberg, 2011). The induction of apoptosis is the major route of cell death that is targeted by many chemotherapeutic drugs, yet it is antagonized by multiple cellular processes, including autophagy.

Autophagy plays dual roles in cancer; it can function as either a tumor suppressor by preventing the accumulation of damaged proteins and organelles or a survival pathway by suppressing apoptosis and promoting the growth of established tumors (Booth et al., 2014; Eisenberg-Lerner et al., 2009; Maiuri et al., 2007; Mariño et al., 2014; Su et al., 2015).

Recent studies have indicated that autophagy represents an important mechanism underlying chemotherapy resistance in leukemia (Sehgal et al., 2015) and in solid cancers (Eisenberg-Lerner et al., 2009; Sehgal et al., 2015), although the exact molecular mechanism underlying the effects of autophagy on tumorigenesis must be further elucidated.

Here, we propose a role for promyelocytic leukemia protein (PML) in the negative regulation of autophagy. PML is a tumor suppressor that was initially identified because of its dysregulation during the pathogenesis of acute promyelocytic leukemia (APL) (Piazza et al., 2001). The fusion oncoprotein PML/RARα can activate constitutive autophagy in APL cells, thereby contributing to the anti-apoptotic function of PML/RARα. However, the precise mechanisms by which PML regulates autophagy remain unknown.

Because PML dysregulation is associated with an extensive range of malignancies, including solid tumors (Gurrieri et al., 2004), we reasoned that completely understanding all of the molecular pathways that require PML for the control of cell death and, consequently, of cancer progression is fundamental.

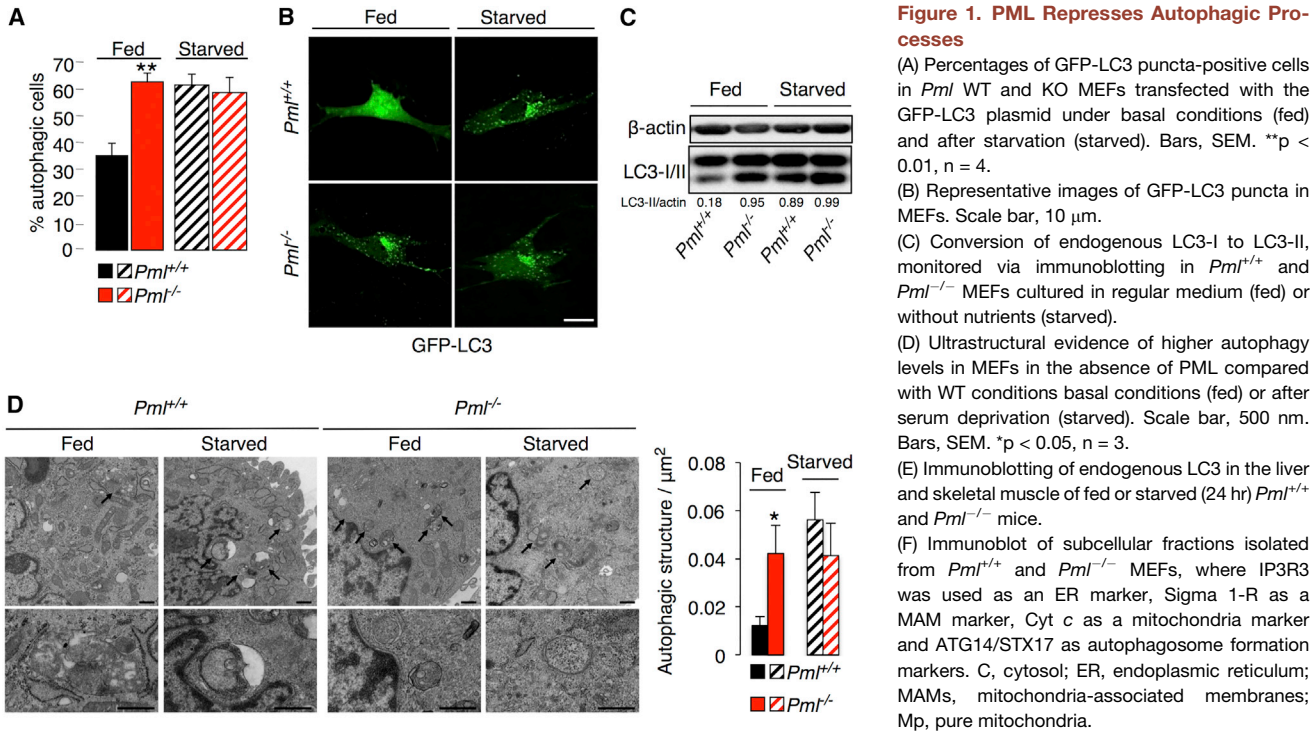

Figure 1. PML Represses Autophagic Processes

(A) Percentages of GFP-LC3 puncta-positive cells in *Pml* WT and KO MEFs transfected with the GFP-LC3 plasmid under basal conditions (fed) and after starvation (starved). Bars, SEM. **p < 0.01, n = 4.

(B) Representative images of GFP-LC3 puncta in MEFs. Scale bar, 10 μm.

(C) Conversion of endogenous LC3-I to LC3-II, monitored via immunoblotting in $Pml^{+/+}$ and $Pml^{-/-}$ MEFs cultured in regular medium (fed) or without nutrients (starved).

(D) Ultrastructural evidence of higher autophagy levels in MEFs in the absence of PML compared with WT conditions basal conditions (fed) or after serum deprivation (starved). Scale bar, 500 nm. Bars, SEM. *p < 0.05, n = 3.

(E) Immunoblotting of endogenous LC3 in the liver and skeletal muscle of fed or starved (24 hr) $Pml^{+/+}$ and $Pml^{-/-}$ mice.

(F) Immunoblot of subcellular fractions isolated from $Pml^{+/+}$ and $Pml^{-/-}$ MEFs, where IP3R3 was used as an ER marker, Sigma 1-R as a MAM marker, Cyt *c* as a mitochondria marker and ATG14/STX17 as autophagosome formation markers. C, cytosol; ER, endoplasmic reticulum; MAMs, mitochondria-associated membranes; Mp, pure mitochondria.

RESULTS

PML Represses the Autophagic Process

To determine the possible involvement of Pml in the autophagic process, we monitored autophagosome levels in wild-type ($Pml^{+/+}$) and $Pml^{-/-}$ primary mouse embryonic fibroblasts (MEFs) either under normal conditions (fed) or after serum deprivation (starved). Autophagosomes were detected in live-imaging experiments as fluorescent cytoplasmic dots that concentrated microtubule-associated proteins 1 light chain 3A (MAP1LC3A, best known as LC3) fused to GFP. Such GFP-LC3-positive dots were more frequent in $Pml^{-/-}$ MEFs than in wild-type (WT) MEFs under basal conditions (Figures 1A and 1B). The redistribution of LC3 to autophagosomes is usually accompanied by its lipidation, causing an increase in its electrophoretic mobility (and hence a shift from LC3-I to LC3-II) (Klionsky et al., 2012). Accordingly, detection of the conversion of LC3-I to LC3-II via immunoblotting confirmed that $Pml^{-/-}$ MEFs contained higher levels of LC-3-II than WT MEFs under basal conditions (Figure 1C). Following nutrient deprivation, autophagosome formation was induced in WT MEFs at levels similar to those found in $Pml^{-/-}$ cells under fed conditions; conversely, autophagosome formation did not significantly change after starvation and other pro-autophagic stimuli in $Pml^{-/-}$ MEFs (Figures 1A–1C and S1A). Transmission electron microscopy (TEM) confirmed the increase in baseline autophagosomes in $Pml^{-/-}$ MEFs (Figure 1D).

Increased LC3-II abundance was also detected in the liver and skeletal muscle of adult $Pml^{-/-}$ mice (Figure 1E) compared with WT animals. Interestingly, as observed above in vitro, LC3-II could be induced via starvation (food deprivation for 24 hr) only in WT mice (but not in $Pml^{-/-}$ mice), in which LC3-II reached the same level as that observed in $Pml^{-/-}$ mice under fed conditions. Thus, we analyzed whether *Pml* might affect the formation of autophagosomes. We found that two autophagosome markers, ATG14 and STX17 (Hamasaki et al., 2013), were shifted to the MAM compartments in $Pml^{-/-}$ MEFs, suggesting increased autophagosome biogenesis in the absence of *Pml* (Figures 1F and S1B).

Control experiments revealed that short hairpin RNA (shRNA)-mediated knockdown of *Pml* also increased the number of GFP-LC3 puncta in WT MEFs, while reintroduction of PML into $Pml^{-/-}$ MEFs reduced GFP-LC3 puncta (Figures S1C and S1D). Pharmacological blockade of autophagy using 3-methyladenine (3-MA), an inhibitor of the Beclin-1 (Becl1)-dependent

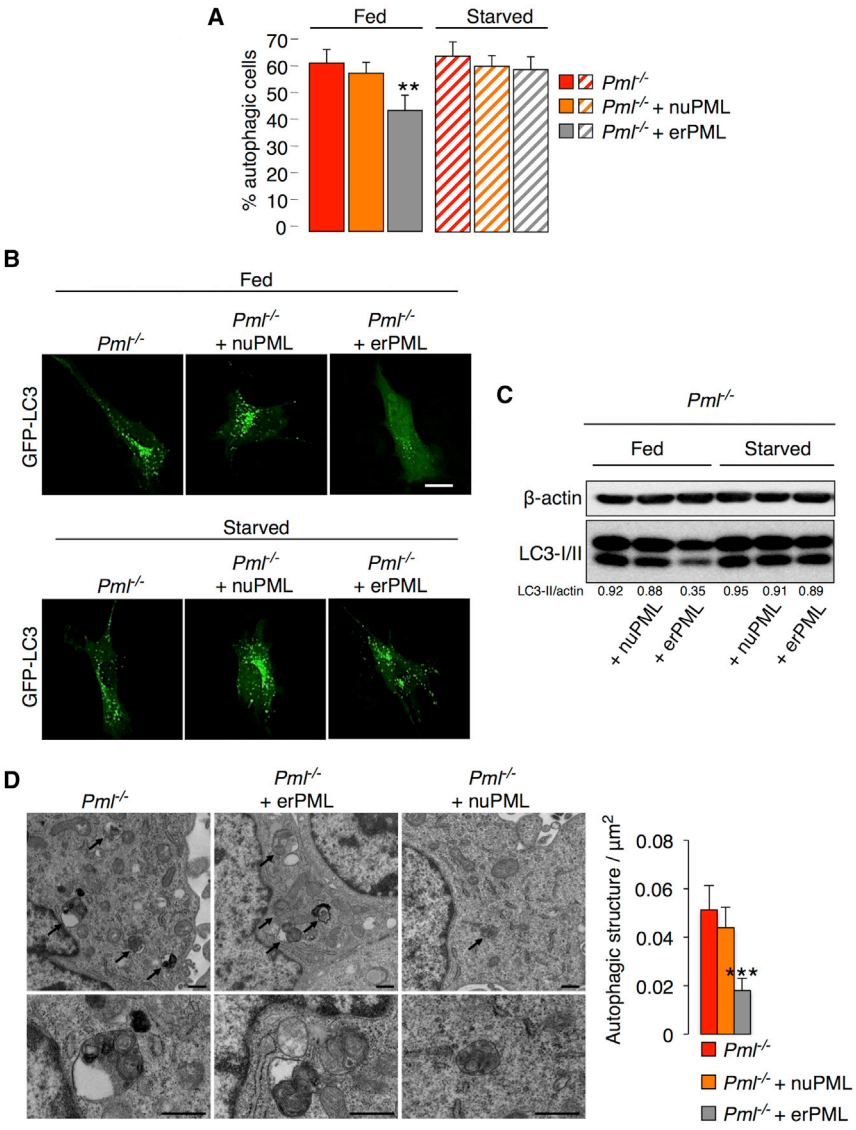

Figure 2. PML Localization at ER/MAM Domains Controls the Levels of Autophagy

(A) Percentages of GFP-LC3 puncta-positive cells induced by the transfection of erPML and nuPML chimeras into $Pml^{-/-}$ MEFs under resting conditions (fed) and after serum deprivation (starved). Bars, SEM. **$p < 0.01$, $n = 4$.

(B) Representative images of GFP-LC3 puncta in $Pml^{-/-}$ MEFs before and after re-introduction of the two chimeras, erPML and nuPML. Scale bar, 10 μm.

(C) Immunoblotting to detect LC3 in PML KO MEFs after the re-introduction of erPML and nuPML chimeras both under basal conditions (fed) and after serum deprivation (starved).

(D) Images of autophagic ultrastructures in $Pml^{-/-}$ MEFs following the transfection of erPML and nuPML chimeras. Scale bar, 500 nm. Bars, SEM. ***$p < 0.005$, $n = 3$.

class III phosphoinositide 3-kinase (PI3K), blocked the excessive formation of autophagosomes in $Pml^{-/-}$ MEFs, indicated by the similar amounts of LC3-GFP puncta contained in WT and $Pml^{-/-}$ MEFs (Figure S1E). Accordingly, knockdown of Becl1 with two distinct shRNAs (Boya et al., 2005) reduced the levels of LC3-II in $Pml^{-/-}$ MEFs (Figure S1F). Conversely, in vivo blockade of the last step of autophagy (which depends on lysosomal proteases) by means of leupeptin (Esteban-Martínez and Boya, 2015) failed to reduce the difference in LC3-II formation observed between WT and $Pml^{-/-}$ mouse livers (Figure S1G). Similarly, bafilomycin A1 or NH_4Cl, which both abolish the acidification of lysosomes, caused an increased abundance of LC3-II in both WT and $Pml^{-/-}$ MEFs, yet it did not abolish the difference in LC3-II formation between MEFs with the two genotypes, suggesting that the absence of *Pml* truly induces an increase in autophagic flux (Figures S1H and S1I).

PML Localization at Endoplasmic Reticulum/MAM Contact Sites Is Necessary for Modulating Autophagy

The localization of PML at ER/MAM contact sites (Figures S2A–S2C) is fundamental for its pro-apoptotic activity via a calcium (Ca^{2+})-mediated pathway (Giorgi et al., 2010). Driven by this consideration, we determined whether PML also plays a role in the control of autophagy in these specialized domains. To address this question, we took advantage of an erPML chimeric protein, which contains the entire PML protein targeted to the outer surface of the ER (Figure S2D) and can rescue sensitivity to apoptosis in $Pml^{-/-}$ MEFs (Giorgi et al., 2010). ErPML (but not a control construct targeted to nuclei, nuPML) localized at MAMs and suppressed the elevated levels of autophagy when re-introduced into $Pml^{-/-}$ MEFs (Figures 2A–2D) comparable to those measured in WT MEFs (Figure 1). $Pml^{-/-}$ MEFs re-transfected with erPML (but not with nuPML) acquired the ability to increase autophagy in response to starvation (Figures 2A–2C). Hence, the presence of PML at MAMs may be important for the repression of autophagy. Accordingly, nutrient deprivation-dependent autophagy induction in WT cells was accompanied by the delocalization of Pml from ER-mitochondria contact sites (Figure S2E).

p53 Drives PML Localization at MAMs

Previously, the role of p53 in the regulation of autophagy was proposed to depend on its localization (Tasdemir et al., 2008). Cytoplasmic p53, particularly when associated with the ER membranes, represses basal pro-survival autophagy, whereas nuclear p53 fails to do so (Tasdemir et al., 2008). However, the precise molecular mechanism by which p53 suppresses autophagy remains elusive.

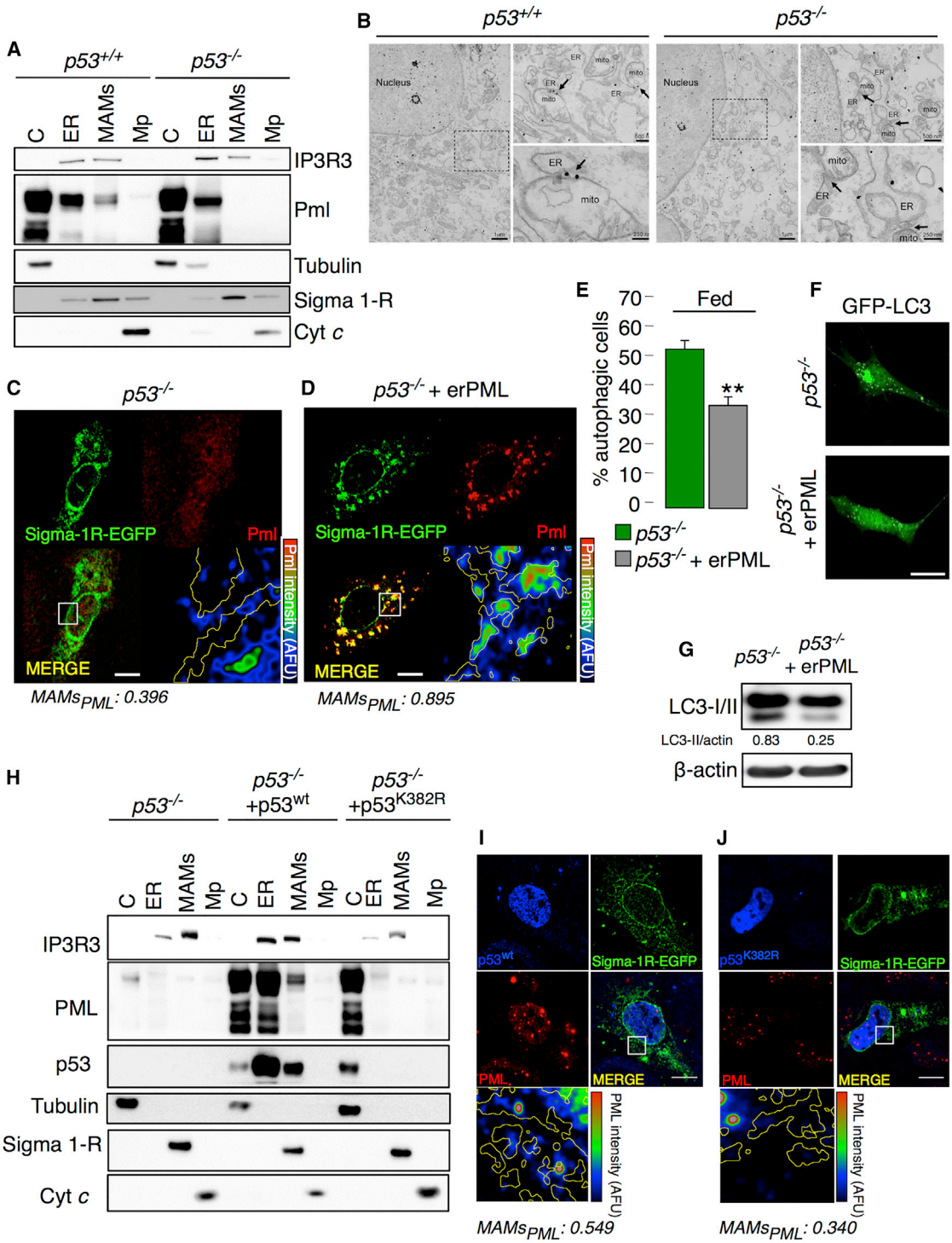

Figure 3. Delocalization of PML from the MAMs Is p53 Dependent

(A) Immunoblot detection of PML in $p53^{-/-}$ MEF fractions. C, cytosol; ER, endoplasmic reticulum; MAMs, mitochondria-associated membranes; Mp, pure mitochondria.

(B) Pre-embedding immunogold labeling of PML in $p53^{+/+}$ and $p53^{-/-}$ MEFs. In WT cells, PML localizes mainly at discrete sites in the nucleus (PML nuclear bodies) and on the ER, outer mitochondria membrane (OMM) and MAMs (arrows indicate PML-positive MAMs). In $p53^{-/-}$ MEFs, while PML still localizes at PML nuclear bodies and on the ER membranes, the association with OMM and in particular the presence at MAMs is reduced (arrows indicate PML negative MAMs). Scale bar, left panel, 1 μm; upper-right panel, 500 nm; lower-right panel, 250 nm.

(legend continued on next page)

Because of the tight interaction between p53 and PML (Ablain et al., 2014; Guo et al., 2000; Papa et al., 2012; Pearson and Pelicci, 2001), we sought to investigate the possible effect of PML on autophagy in relation to p53. Therefore, we evaluated p53 and PML localization at points of close contact between the ER and mitochondria in $Pml^{-/-}$ and $p53^{-/-}$ backgrounds, respectively. Subcellular fractionation of MEFs with distinct genotypes revealed that p53 protein was associated with MAMs irrespective of the absence or presence of Pml (Figure S3A), suggesting that Pml does not control the subcellular localization of p53. In stark contrast, in the absence of p53, Pml delocalized from MAMs without an overall change in its expression (Figures S3B and S3C), as shown by comparative subcellular fractionation followed by immunoblots, immunogold detection by electron microscopy (EM) and immunofluorescence (IF) analyses of WT and $p53^{-/-}$ MEFs (Figures 3A–3C and S3D). These results suggest that PML might function as a master regulator of autophagy downstream of p53.

This concept was confirmed by the introduction of the erPML chimera into $p53^{-/-}$ MEFs. Indeed, the forced localization of Pml at MAMs in $p53^{-/-}$ cells (Figure 3D) reduced autophagosome formation (Figures 3E–3G). Similarly, the re-introduction of $p53^{wt}$, which also localizes at the ER and MAMs (Giorgi et al., 2015b), engages PML at those contact sites (Figures 3H, 3I, and S3E) and suppresses signs of enhanced autophagy in $p53^{-/-}$ cells (Figures S3F and S3G). Furthermore, a p53 mutant ($p53^{K382R}$) that is unable to inhibit autophagy when re-introduced into $p53^{-/-}$ cells (Morselli et al., 2011) (Figures S3F and S3G) failed to localize at the ER/MAMs in $p53^{-/-}$ cells and also failed to rescue Pml localization to MAMs (Figures 3H, 3J, and S3H). Intriguingly, we observed, by means of proximity ligation assay (PLA), that PML interacts with $p53^{wt}$ in large extent in the nucleus, but also in regions enriched of MAMs marker (Figure S3I). Accordingly, this ability is lost in cells expressing the $p53^{K382R}$ as this mutant is also reported to have reduced ability to bind PML (Pearson et al., 2000). Overall, these results strongly suggest that p53 maintains proper Pml localization at MAM domains that is fundamental for the repression of autophagy.

Pml Controls Autophagy through the AMPK/mTOR/Ulk1 Pathway

Autophagy is activated as a pro-survival mechanism in response to various cellular stresses associated with an insufficient energy supply (Amaravadi et al., 2011; Galluzzi et al., 2014). The autophagy-signaling network is controlled by a variety of kinases. In particular, a complex that includes AMP-activated protein kinase (AMPK), mammalian target of rapamycin (mTOR), and unc-51-like kinase 1 (Ulk1) has emerged as important for the regulation of autophagy (Kim et al., 2011; Nazio et al., 2013). Thus, we examined the relationship between PML-dependent autophagy and this multiprotein complex.

AMPK is a conserved energy-sensing kinase that is activated by phosphorylation in response to low cellular energy levels (Mihaylova and Shaw, 2011). Previously, we reported that, in the absence of PML, cells produced less ATP after agonist stimulation (Giorgi et al., 2010). As the ratio of AMP to ATP represents an important means of regulating the activity of AMPK, we examined the role of AMPK by quantifying its phosphorylation. As expected, $Pml^{-/-}$ MEFs exhibited increased levels of phosphorylated AMPK (Figure 4A), which correlated with enhanced autophagy, compared with that of WT MEFs. Accordingly, the downstream AMPK substrate acetyl CoA carboxylase was hyper-phosphorylated (Figure 4A). Higher levels of AMPK phosphorylation, correlating with increased autophagy, were also observed in the liver and skeletal muscle of adult $Pml^{-/-}$ mice compared to WT (Figure 4B).

In contrast to AMPK, mTOR activity reflects a higher energy status with the consequent inhibition of autophagy (Kim et al., 2011). AMPK and mTOR have recently been proposed to regulate autophagy through the coordinated phosphorylation of Ulk1 (Egan et al., 2011; Kim et al., 2011). To determine whether AMPK activation in the absence of Pml promotes autophagy by activating Ulk1, we examined the phosphorylation levels of both Ulk1 and mTOR. In agreement with the findings of Kim et al. (2011), increased levels of LC3 lipidation in either $Pml^{-/-}$ cells or Pml KO mice tissues were associated with Ulk1 hyper-phosphorylation (which reflects Ulk1 activation), together with reduced phosphorylation of mTOR and its substrate $p70^{S6K}$ (which reflects mTOR inhibition) (Figures 4A and 4B). These results are consistent with the possibility that PML controls autophagy through the AMPK/mTOR/Ulk1 pathway.

The critical role of Ca^{2+} in the formation of autophagosomes has recently been emphasized (Cárdenas et al., 2010). In addition to a high concentration of AMP, AMPK activity is upregulated through the inhibition of mitochondrial Ca^{2+} uptake due to reduced Ca^{2+} release via the inositol triphosphate receptor (IP3R) (Cárdenas et al., 2010). $Pml^{-/-}$ cells display a reduced Ca^{2+} transfer from the ER to mitochondria via IP3R, which protects cells from apoptosis (Giorgi et al., 2010). To verify whether downregulated ER-mitochondrial Ca^{2+} transfer is important for

(C and D) The co-localization of PML (red) and Sigma 1-R-EGFP (used as a MAM marker, green) in (C) $p53^{-/-}$ MEFs and in (D) $p53^{-/-}$ MEFs following re-introduction of the erPML chimera was analyzed based on immunofluorescence using confocal images. The lower-left panels display the merged image of the two stains. The lower-right panels display the PML signal overlaid with MAMs (MAM boundaries are highlighted in yellow) in a rainbow lookup table (LUT) (MAMsPML: Manders coefficient for PML staining was calculated according to Manders coefficient method as the proportion of PML signal overlapping with the Sigma 1-R marker). Scale bar, 10 μm.

(E–G) Reduced levels of autophagy were observed in $p53^{-/-}$ MEFs following erPML transfection as determined based on the percentage of LC3-GFP puncta (E and F) and on immunoblotting to detect LC3-I conversion into LC3-II (G). Representative images are shown. Bars, SEM. $^{**}p < 0.01$, n = 4. Scale bar, 10 μm.

(H) PML and p53 localization following the re-introduction of $p53^{wt}$ as analyzed via immunoblotting in H1299 $p53^{-/-}$ cell fractions, where IP3R3 was used as an ER marker, Sigma 1-R as a MAM marker, Tubulin as a cytosolic marker and Cyt *c* as a mitochondria marker. C, cytosol; ER, endoplasmic reticulum; MAMs, mitochondria-associated membranes; Mp, pure mitochondria.

(I and J) Immunofluorescence of Pml (red) and p53 (blue) in H1299 cells after the re-introduction of $p53^{wt}$ (I) and mutant $p53^{K382R}$ (J). The lower-left panels display the merged image of the two stains. The lower-right panels display the Pml signal overlaid with MAMs (MAM boundaries are highlighted in yellow) in a rainbow LUT. Scale bar, 10 μm.

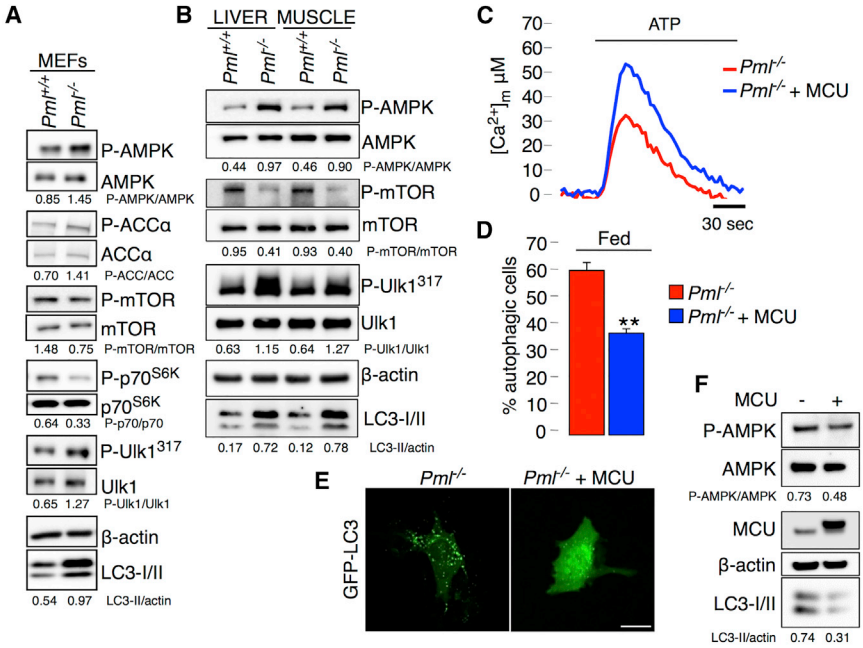

Figure 4. PML Modulates Autophagy through the AMPK/mTOR/Ulk1 Pathway in a Ca^{2+}-Dependent Manner

(A) Immunoblot detection of the phosphorylation status of AMPK, ACCα, $p70^{S6K}$, mTOR, and Ulk1 in $Pml^{+/+}$ and $Pml^{-/-}$ MEFs.

(B) Detection of autophagy and AMPK-mTOR-Ulk1 phosphorylation levels in the liver and skeletal muscle of $Pml^{+/+}$ and $Pml^{-/-}$ mice.

(C) Representative traces of increased mitochondrial Ca^{2+} levels in $Pml^{-/-}$ MEFs after MCU overexpression. $Pml^{-/-}$: $[Ca^{2+}]_m$ peak 33.7 ± 2.55; $Pml^{-/-}$ + MCU: $[Ca^{2+}]_m$ peak 59.2 ± 6.22) SEM. **p < 0.01, n = 3.

(D–F) Quantification of autophagy in $Pml^{-/-}$ MEFs following MCU overexpression via (D and E) analysis of GFP-LC3 puncta or (F) immunoblotting. Representative images are shown. Bars, SEM. **p < 0.01, n = 3. Scale bar, 10 μm.

(G) Schematic model of autophagy regulation by PML. In the absence of Pml, the release of Ca^{2+} from the ER into the mitochondria and the production of ATP are reduced. This low-energy status induces AMPK activation, mTOR inhibition, and Ulk1 phosphorylation, leading to increased autophagy.

the induction of autophagy in $Pml^{-/-}$ cells, we increased mitochondrial Ca^{2+} uptake in $Pml^{-/-}$ cells by overexpressing the mitochondrial Ca^{2+} uniporter (MCU) (Baughman et al., 2011; De Stefani et al., 2011). MCU overexpression in $Pml^{-/-}$ MEFs increased the ability of mitochondria to accumulate Ca^{2+} (Figure 4C) and was sufficient to repress autophagy (Figures 4D–4F) by reducing the amount of activated AMPK (Figure 4F), suggesting that PML controls autophagy at ER-mitochondria contact sites by its effects on Ca^{2+} homeostasis (Figure 4G).

Loss of PML Enhances Resistance to Metabolic Stress

As a homeostatic process, autophagy plays a crucial role during metabolic stress in an attempt to maintain/restore cellular homeostasis (Degenhardt et al., 2006; Rabinowitz and White, 2010). Upon starvation, WT cells exhibited a rapid decrease in ATP production, as demonstrated previously (Tasdemir et al., 2008), whereas cells lacking PML maintained high ATP levels during stress (Figure 5A). Accordingly, $Pml^{-/-}$ cells maintained a higher mitochondrial membrane potential (Ψ_m) under stress conditions compared to WT controls (Figure 5B). This autophagy-dependent energized status of *Pml* KO cells conferred enhanced resistance to cell death (Figure 5C), favoring cell growth under unfavorable conditions (Figure 5D), such as those present in tumors.

We confirmed this energized status of *Pml* KO cells by analyzing mitochondrial function in response to metabolic stress. The oxygen consumption rate (OCR) was used as readout of mitochondrial basal respiration and ATP-linked respiration in $Pml^{+/+}$ and $Pml^{-/-}$ MEFs. As shown in Figure 5E, the loss of PML under basal conditions induced only a minor reduction in basal and ATP-dependent OCRs. Interestingly, when MEFs were deprived from glucose, WT cells displayed a dramatic reduction in both basal and ATP-dependent OCRs, while the OCR was only slightly affected in $Pml^{-/-}$ cells.

Accordingly, either genetic inhibition of autophagy (*Becn1* shRNA) or re-introduction of the erPML chimera into $Pml^{-/-}$ MEFs prevented the protection of such cells from death under glucose-depleting conditions (Figures S4A–S4D). These results indicate that enhanced autophagy is responsible for the resistance of PML-deficient cells to nutrient stress.

Targeting Autophagy in PML-Null Cells Rescues Chemotherapy-Induced Cell Death

Accumulating evidence has indicated that malignant cells in established tumors utilize autophagy to resist chemotherapy-induced

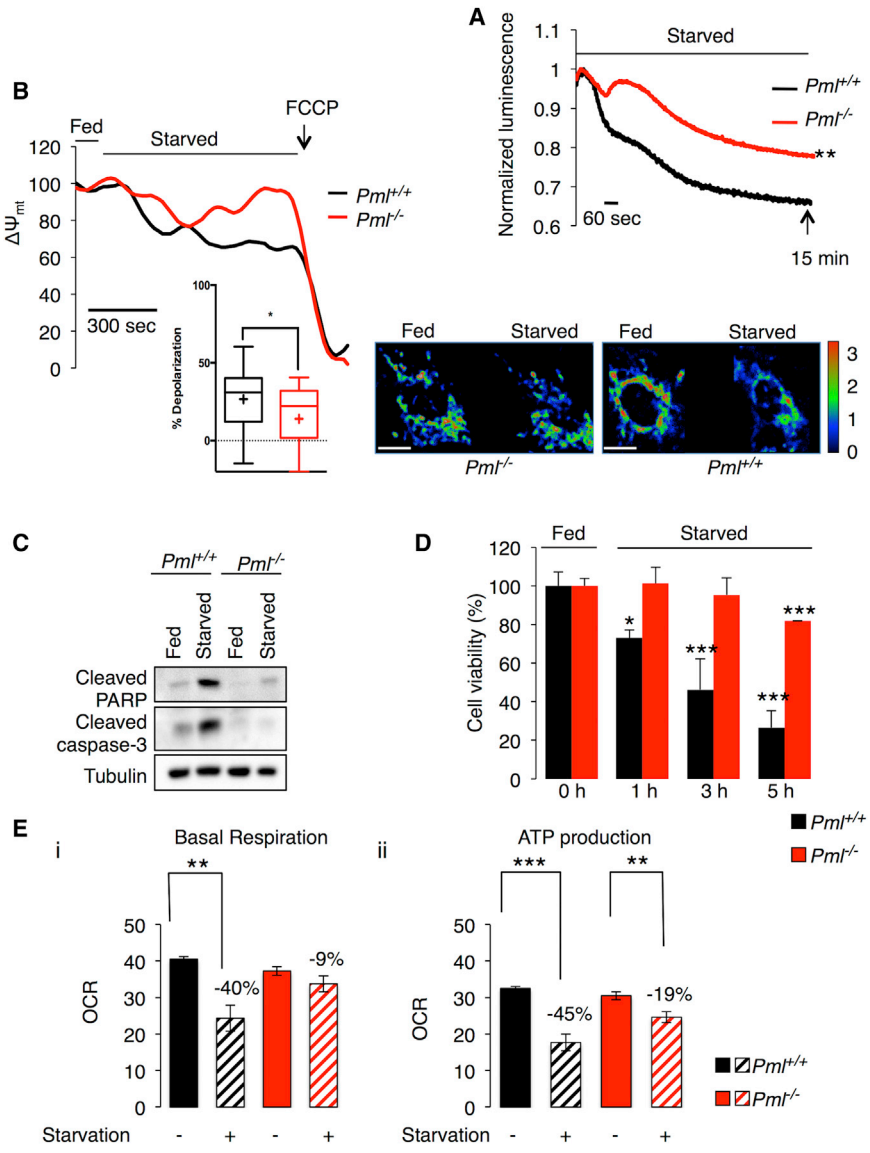

Figure 5. PML Deletion Favors Cell Survival under Stress Conditions Due to Autophagy Activation

(A) Cytosolic ATP levels in $Pml^{+/+}$ and $Pml^{-/-}$ MEFs as measured by luciferase expression under starvation conditions (glucose deprivation for 15 min). **p < 0.01, compared to WT conditions, n = 3.

(B) Analysis of mitochondrial membrane potential (Ψ_m) as measured by TMRM intensity in $Pml^{+/+}$ and $Pml^{-/-}$ MEFs. Where indicated, cells were deprived of glucose or exposed to 1 μM carbonilcyanide p-triflouromethoxyphenylhydrazone (FCCP). On the bottom-right side, representative images of the TMRM signal in the presence or absence of glucose are shown. Normalized TMRM intensity is displayed as a rainbow LUT (statistical analysis cross, average; line, median; box, 25 and 75 percentile; bars, maximum and minimum values; *p < 0.05, n = 3). Scale bar, 10 μm.

(C and D) $Pml^{-/-}$ cells are more resistant to metabolic stress-induced cell death than $Pml^{+/+}$ cells as confirmed by (C) immunoblot for apoptotic markers and by (D) cell viability assay. Metabolic stress is induced by glucose deprivation (3 hr for western blot and the indicated hours for cell viability). Bars, SEM. *p < 0.05, ***p < 0.005, n = 3.

(E) Basal-dependent (i) and ATP synthase-dependent (ii, + Oligomycin) mitochondrial O_2 consumption rates (OCR) in $Pml^{-/-}$ and $Pml^{+/+}$ MEFs under starvation conditions (glucose, pyruvate, and glutamine deprivation for 1 hr). Bars, SEM. **p < 0.01, ***p < 0.005, n = 4.

cell death. Indeed, solid tumors in particular develop regions of hypoxia and limited nutrient availability in their centers, creating a microenvironment of metabolic stress. Under these hostile conditions, autophagy activation promotes cell survival by providing missing nutrients (Maes et al., 2013; Xu et al., 2013). Accordingly, the inhibition of autophagy augments the response of tumor cells to anticancer drugs (Chittaranjan et al., 2014; Sehgal et al., 2015; Selvakumaran et al., 2013).

To confirm the role of PML in adaptation to metabolic stress, we directly analyzed autophagy levels, mitochondrial respiration, and PML localization in human NB4 promyelocytic leukemia cells expressing the PML-RARα oncogenic fusion protein, which causes neoplastic transformation by disrupting the function of PML.

Treatment with arsenic trioxide (ATO), typically used in APL therapy to degrade the PML-RARα (Lallemand-Breitenbach et al., 2001), modulated autophagic machinery in NB4 cells (Figures 6A–6C). Interestingly, we found that short-term treatment of ATO, promoting the selective proteasome-dependent degradation of PML-RARα fusion protein but not of PML, led to an increase in both p62 and LC3-II levels, indicating a block in the autophagic process (Figure 6C). Accordingly, treatment with an inhibitor of autophagic flux, reported in Figure 6D, suggested that ATO interferes with autophagosome clearance (Ren et al., 2011) and thus reverts the APL condition through reduced autophagy efficacy.

Moreover, NB4 cells displayed a higher resistance to metabolic stress (by means of measurements of oxygen consumption during substrate deprivation) that reverted after ATO treatment (Figure 6E), which also restored proper PML localization at ER/MAM contact sites already in the leukemia background (Figure 6F).

To further analyze the role of PML in cancer development, we compared the sensitivity of $Pml^{+/+}$ and $Pml^{-/-}$ MEFs to the chemotherapeutic agent 5-fluorouracil (5-FU) (Li et al., 2010). As expected, $Pml^{-/-}$ cells were protected from apoptosis (Giorgi et al., 2010) compared to WT cells (Figures 7A and 7B). Pharmacological inhibition of autophagy by either 3-methyladenine (3-MA) or the antimalarial drug chloroquine (CQ) (Figure S5A)

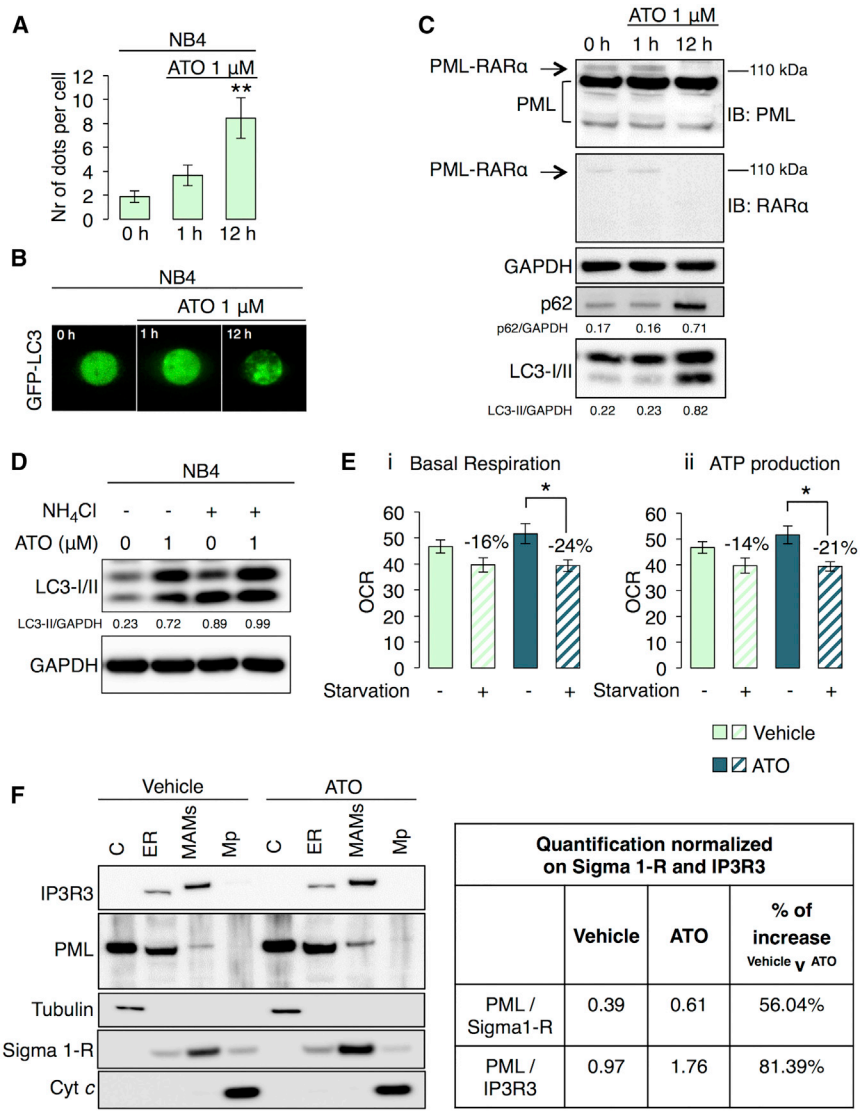

Quantification normalized on Sigma 1-R and IP3R3			
	Vehicle	ATO	% of increase Vehicle v ATO
PML / Sigma1-R	0.39	0.61	56.04%
PML / IP3R3	0.97	1.76	81.39%

Figure 6. Selective Degradation of the PML-RARα Oncogenic Fusion Protein in APL Human Cancer Restores a Correct PML Localization and the Sensitivity to Metabolic Stress

(A) Quantification of LC3 dots in NB4 cells transfected with the GFP-LC3 plasmid under basal conditions (0 hr) and after ATO (1 μM) treatment. Bars, SEM. **$p < 0.01$, $n = 4$.

(B) Representative images of GFP-LC3 dots showing the effects of ATO on autophagic process in NB4 cells.

(C) PML-RARα degradation and LC3-II and p62 accumulation after ATO treatment (1 μM) in NB4 cells. PML-RARα was detected monitoring the band at 110 kDa either with a PML antibody or with a RARα antibody.

(D) Analysis of autophagic flux in NB4 cells after ATO treatment (1 μM).

(E) Quantification of basal (i) and Oligomycin ATP synthase-dependent (ii) mitochondrial O_2 consumption rates (OCR) either in vehicle or ATO treated NB4 cells under starvation conditions (glucose, pyruvate, and glutamine deprivation for 1 hr). Bars, SEM. *$p < 0.05$, $n = 7$.

(F) Immunoblot of subcellular fractions isolated from NB4 cells and PML protein quantification at MAM regions and ER normalized to the amount of Sigma 1-R and IP3R3. Where indicated, cells were exposed to ATO treatment (1 μM, 12 hr). IP3R3, Sigma 1-R and Cyt c was used as ER, MAMs, and mitochondria marker, respectively.

alone did not alter cell viability, yet it markedly increased apoptosis when combined with 5-FU, and this effect was particularly remarkable for *Pml*$^{-/-}$ MEFs (Figures 7A and 7B).

Next, we explored whether the synergistic effect of CQ and 5-FU was also applicable in vivo. Transformed *Pml*$^{+/+}$ and *Pml*$^{-/-}$ MEFs that displayed levels of autophagy comparable to those of primary cells (Figure S5B) were injected subcutaneously either into immunodeficient *nu/nu* mice or in syngeneic mice, and the resultant tumor volumes were monitored. *Pml*$^{-/-}$ cells exhibited a particularly high tumorigenic potential both in vitro (Figures S5C–S5E) and in vivo (Figures 7C and S5F), developing tumors that were 10-fold larger than those generated from WT cells (Figures 7C, 7D, and S5G) and with elevated signs of autophagy (Figures 7E and S5H).

Compared with the control conditions (PBS), 5-FU treatment slightly suppressed tumor growth, whereas 5-FU combined with CQ greatly reduced the sizes of *Pml*$^{-/-}$ tumors (Figures 7C and 7D). Treatment with CQ alone had no significant effects on tumor growth (Figures S5I and S5J). Genetic inhibition of autophagy (by means of *Becn1* shRNA) in *Pml*$^{-/-}$ cells reduced their tumorigenic potential either in vitro (Figures S6A and S6B) or in vivo (Figures S6C and S6D) and restored their sensitivity to chemotherapy (Figure S6E).

Intravenous injection of a fluorescent probe (SR-FLIVO) was used to detect apoptosis-associated caspase activation within the tumors (Giorgi et al., 2015a). *Pml*$^{-/-}$ tumors were completely insensitive to 5-FU-induced apoptosis (Figure 7F), correlating with higher levels of autophagy (Figure 7E), yet they responded to the combined treatment with 5-FU and CQ by vigorous apoptosis induction (Figure 7F) and immunoblot-detectable caspase-3 maturation (Figure 7G). Knockdown of Beclin-1 in *Pml*$^{-/-}$ cells led to the generation of tumors that contained areas undergoing apoptosis (Figures S6F and S6G) and that were less abundant in *Pml*$^{-/-}$ tumors transfected with a scrambled control shRNA. Hence, elevated autophagy may be responsible for the growth advantage of *Pml*$^{-/-}$ cancers. Indeed, in human colonic adenocarcinoma samples with reduced PML protein expression, levels of LC3 detectable by immunohistochemistry were relatively higher compared to those found in cancer tissues with PML protein abundance (Figure 7H).

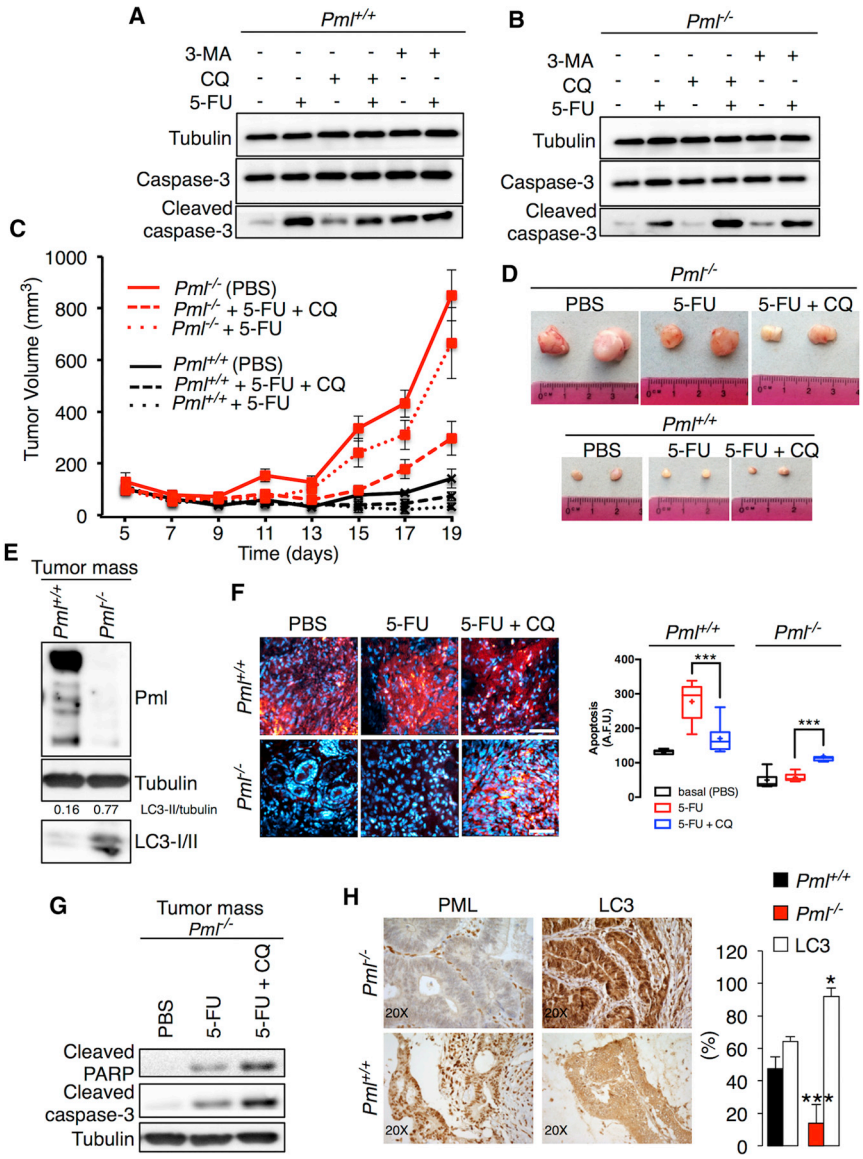

Figure 7. Inhibition of Autophagy Augments the Cytotoxicity of Chemotherapy Treatment in Pml KO Tumors

(A and B) $Pml^{+/+}$ MEFs are sensitive to 5-fluoracil-induced cell death (5-FU, 25 μM for 16 hr), whereas $Pml^{-/-}$ cells are resistant. Inhibition of autophagy by treatment with 3-MA (2.5 mM for 16 hr) or CQ (5 μM for 16 hr) increases apoptosis induced via chemotherapy treatment with 5-FU (25 μM for 16 hr) in $Pml^{-/-}$ MEFs.

(C) Tumor growth of $Pml^{-/-}$ and $Pml^{+/+}$ transformed MEF xenografts.

(D) Representative images of mouse fibrosarcoma xenografts.

(E) Increased levels of autophagy in tumors derived from $Pml^{-/-}$-transformed MEFs as analyzed by immunoblotting. Tumors were excised on day 19 after inoculation.

(F) Analysis of apoptosis based on the intensity of fluorescence (SR-FLIVO) emitted in tumor tissue sections, accompanied by statistical analysis (cross, average; line, median; box, 25 and 75 percentile; bars, maximum and minimum values; ***$p < 0.005$, $n = 3$). Scale bar, 50 μm.

(G) Increased cytotoxicity-chemotherapy effects on $Pml^{-/-}$ tumors after autophagy inhibition.

(H) Representative histological sections of human colon cancer immunostained for PML and LC3 accompanied by statistical analysis expressed as the percentage of staining intensity. Bars, SEM. *$p < 0.05$, ***$p < 0.005$, $n = 13$. Magnification 20×.

DISCUSSION

Loss of PML Confers a Metabolic Advantage to Cells under Nutrient Deprivation

Autophagy is an important homeostatic mechanism with a paradoxical dual role: it can function as a cell survival pathway, suppressing apoptosis, or it can lead to death. As a result, the connection between autophagy and apoptosis is complex and affects the treatment of diseases associated with cell death. Alteration of the autophagic machinery is associated with various human disorders, establishing autophagy as a therapeutic target (i.e., a target for drug development). The connection of autophagy with the development of cancer has been well established, although the exact roles played by this process during various stages of tumor progression are not yet clear and, in some cases, are contradictory.

Here, we provide molecular insight into the acquisition of tumor-promoting behavior due to the loss of the PML protein. *Pml* is a tumor suppressor gene that was originally related to the pathogenesis of acute promyelocytic leukemia (APL). However, the loss of PML was later found to be a critical event in various human cancers (Gurrieri et al., 2004). We recently identified an extra-nuclear transcription-independent function of PML in regulating cell survival through changes in Ca^{2+} signaling at ER/mitochondria contact sites (Giorgi et al., 2010). Accumulating evidence has suggested that ER and MAM domains play a prominent role in autophagy (Hamasaki et al., 2013; Heath-Engel et al., 2008) and emphasized the important role of IP3R and Ca^{2+} in autophagosome formation (Cárdenas et al., 2010; Criollo et al., 2007); therefore, we sought to investigate the role of PML in these processes.

We clearly demonstrated that the localization of PML at the ER-mitochondria contact sites is fundamental not only for apoptosis control, but also for autophagy regulation. At these sites, PML represses autophagosome formation and, thus, autophagy induction. We found that the mislocalization of PML away from MAMs is necessary to activate autophagy in response to stress and that the same mechanism occurs in the absence of p53. Our data demonstrate that p53, which also localizes at ER/MAMs (Giorgi et al., 2015b), operates as a bridge to maintain

the correct localization of PML. $p53^{K382R}$ mutants, which display reduced interactions with PML (Pearson et al., 2000) and are unable to localize at MAMs, cannot preserve PML localization, making them incapable of suppressing autophagy.

PML loss reduced IP3R-mediated Ca^{2+} transfer from the ER to mitochondria. Mitochondrial Ca^{2+} stimulates tricarboxylic acid (TCA) cycle dehydrogenases and subsequent mitochondrial respiration and ATP production. A reduction in $[Ca^{2+}]_m$ inhibits this mechanism that activates AMPK (Cheng et al., 2013). AMPK activates pro-survival autophagy (Cárdenas et al., 2010) by a mechanism involving mTOR (Tasdemir et al., 2008) and Ulk-1 pathways (Kim et al., 2011; Nazio et al., 2013). In our scenario, PML-deprived cells use enhanced baseline levels of autophagy to obtain an advantage during metabolic stress conditions. Indeed, restoration of the Ca^{2+} signal in the context of a $Pml^{-/-}$ or $p53^{-/-}$ background (by overexpression of MCU) restores basal levels of autophagy. Cells lacking PML due to the inhibition of Ca^{2+} release activity have slightly diminished bioenergetics in terms of mitochondrial respiration and ATP production that are sensed by AMPK, which activates autophagy. Because oxygen and glucose supplies are often low in the tumor microenvironment, autophagy, as catabolic process, is necessary to obtain alternative carbons source to preserve normal cellular bioenergetics (Cárdenas et al., 2010) and to confer resistance to cell death to Pml KO cells. Lipid or glutamine catabolism is considered the major alternative pathway to provide carbons for mitochondria (Boroughs and DeBerardinis, 2015). PML promotes lipid utilization by fatty acid oxidation (Carracedo et al., 2013; Ito et al., 2012), excluding this pathway as a possible stimulated carbon source when PML is lost. Furthermore, autophagy can sustain mitochondrial respiration in a glutamine metabolism-dependent manner (Lin et al., 2012; Strohecker et al., 2013). Thus, we could speculate that in the absence of PML, stimulated glutamine catabolism by autophagy is used as an alternative pathway to sustain mitochondrial activity and, thus, cell survival during stress conditions.

These data, together with data presented in our previous publication, indicate that PML from MAMs acts on the transfer of Ca^{2+} from the ER to the mitochondria, thus regulating both apoptosis and autophagy. While the effect on apoptosis is manifested in response to Ca^{2+}-dependent apoptotic stimuli, the stimulation of autophagy is a direct consequence of reduced mitochondrial respiration. Thus, the loss of PML from MAMs confers contemporary resistance to apoptotic stimuli and metabolic stress, promoting cell survival in the tumor environment.

Recent studies have suggested that autophagy represents an important mechanism of resistance to cancer treatments. Therefore, we further investigated the cross-talk between autophagy and PML-related cell death using in vivo models. The prototypical PML-RARα-related promyelocytic leukemia model, NB4, displays low levels of WT PML at MAMs. Exposure to ATO induces degradation of PML-RARα and increased PML levels at MAMs. As a result, ATO-treated cells display blocked autophagy and reduced resistance to metabolic stress. Furthermore, we observed that the absence of PML promotes tumor development associated with resistance to anticancer drugs due to increased autophagy levels in the tumor. Treatment with the autophagy inhibitors 3-MA and CQ restored chemotherapy-related apoptosis. Therefore, our findings hold therapeutic implications for the treatment of solid tumors associated with PML downregulation.

EXPERIMENTAL PROCEDURES

Cell Culture and Transfection

Primary $Pml^{+/+}$ and $Pml^{-/-}$ mouse embryonic fibroblasts (MEFs) and H1299 cells were cultured in DMEM supplemented with 10% fetal bovine serum (FBS) (Life Technologies), 1% penicillin-streptomycin-glutamine (100×) liquid (EuroClone).

Human APL NB4 cells were cultured in RPMI 1640 medium (Gibco) supplemented with 10% FBS (Gibco) and 1% penicillin-streptomycin (100×) liquid (Gibco).

MEFs were transformed with SV40 large T antigen. MEFs were transfected with the following plasmids: PML, erPML, nuPML (Giorgi et al., 2010), $p53^{WT}$, $p53^{K382R}$ (Morselli et al., 2011), MCU (De Stefani et al., 2011), and GFP-LC3 using a MicroPorator (Digital Bio). For PML depletion in WT MEFs, a specific shRNA silencing lentiviral vector (Sigma) was used. H1299 cells were transfected using a standard calcium phosphate procedure with $p53^{WT}$ and $p53^{K382R}$ constructs, while NB4 cells were transfected with a GFP-LC3 plasmid by electroporation.

Procedures involving animals and their care were in conformity with institutional guidelines, and all experimental protocols were approved by the animal ethics committee. $Pml^{+/+}$ and $Pml^{-/-}$ mice were bred and maintained according to both the Federation for Laboratory Animal Science Associations and the Animal Experimental Ethics Committee guidelines.

Autophagy Induction and Inhibition

The autophagic process was triggered in vitro as follows: serum deprivation (EBSS, 1 hr), glucose deprivation (1 hr), rapamycin (100 nM, 24 hr in DMEM with 10% FBS), and lithium treatment (10 mM, 24 hr in DMEM with 10% FBS). Pharmacological inhibition of autophagy was performed by treating cells with 2.5 mM 3-MA (16 hr) or 5 μM CQ (16 hr) in DMEM with 10% FBS (Klionsky et al., 2016; Mizushima et al., 2010). Genetically inhibition of autophagy was performed by using shRNA targeting Beclin1 (psirna42-mbeclin) (Invitrogen). ATO (arsenic trioxide, 1 μM) has been used on NB4 cells for 1 or 12 hr in RPMI with 10% FBS). For in vivo studies on the effects of starvation, mice were deprived of food for 24 hr.

Analysis of Autophagic Flux

Primary $Pml^{+/+}$ and $Pml^{-/-}$ MEFs were treated either with the autophagy inhibitor NH_4Cl (20 mM) or bafilomycin A1 (BafA1, Sigma) (100 nM) in DMEM with 10% FBS (Klionsky et al., 2012; Mizushima et al., 2010). NB4 cells were treated with the autophagy inhibitor NH_4Cl (20 mM) in DMEM with 10% FBS. For in vivo determination of autophagic flux, lysosomal activity was blocked by leupeptin (Boya et al., 2005).

TEM

Primary $Pml^{+/+}$ and $Pml^{-/-}$ MEFs and $Pml^{-/-}$ MEFs expressing nuPML and erPML were cultured in DMEM with 10% FBS and allowed to grow to 70% confluence. Where indicated, the cells were subjected to serum starvation conditions (EBSS, 30 min). After the cells received the indicated treatments, they were fixed in formaldehyde and glutaraldehyde. Fixed samples were post-fixed with osmium tetroxide, dehydrated, and embedded in Araldite Durcupan ACM (Fluka).

Pre-embedding Immunogold Electron Microscopy

Cells were fixed with 4% formaldehyde in 0.1 M phosphate buffer (pH 7.4) for 1 hr at room temperature. Subsequently, cells were permeabilized, blocked, and incubated sequentially with PML primary antibodies (Millipore MAB3738 or Abcam ab72137) and nanogold-conjugated secondary antibodies (Nanoprobes) diluted in blocking buffer. After washes, cells were re-fixed in 1% glutaraldehyde, and nanogold was enlarged with gold enhancement solution (Nanoprobes). Cells were post-fixed with osmium tetroxide, embedded in

epon, and processed into ultrathin slices. After contrasting with uranyl acetate and lead citrate, sections were analyzed with a Zeiss LEO 512 electron microscope.

Aequorin Measurements

All aequorin measurements were performed transfecting cells with the appropriate aequorin chimera targeted to the mitochondria (mtAEQmut), as previously described (Bonora et al., 2013).

Luciferase Measurements

Primary *Pml*$^{+/+}$ and *Pml*$^{-/-}$ MEFs were transfected with cytosolic (untargeted) firefly luciferase, and luminescence was measured as described (Jouaville et al., 1999).

Subcellular Fractionation

Fractionations were performed as described previously (Vance, 1990; Wieckowski et al., 2009). IP3R3, Sigma 1-R, tubulin, and cytochrome *c* (Cyt *c*) were used as markers for the ER, MAMs, cytosol, and pure mitochondria, respectively.

Immunofluorescence Assay

Cells were fixed in 3.7% formaldehyde, washed, permeabilized with 0.1% Triton X-100, and incubated overnight at 37°C in a wet chamber with indicated antibodies. Images were acquired using an LSM 510 laser scanning confocal microscope (Zeiss).

Immunohistochemistry

Four-micrometer-thick sections were cut from formalin-fixed paraffin-embedded blocks. One section for each block was routinely stained with H&E for histological examination. Immunodetection of PML and LC3B was performed using the Multimeric Detection Kit (Universal DAB Detection Kit Ultraview, Roche Tissue Diagnostics) on a BenchMark XT automated immunostainer (Gurrieri et al., 2004; Rosenfeldt et al., 2012).

Measurements of Mitochondrial Membrane Potential

Mitochondrial membrane potential (Ψ_m) was assessed by loading cells with 10 nM tetramethyl rhodamine methyl ester (TMRM; Life Technologies, T-668) for 35 min at 37°C in Krebs-ringer bicarbonate (KRB) supplemented with 1 mM $CaCl_2$. Images were acquired using an inverted confocal microscope.

XF Bioenergetic Analysis

OCRs in *Pml*$^{+/+}$ and *Pml*$^{-/-}$ MEFs and NB4 cells were measured using a Seahorse XF96 instrument (Seahorse Biosciences) according to the manufacturer's protocols.

Cell Proliferation and Viability Assay

Cells seeded in 6-well plates in triplicate and allowed to grow to 80% confluence were exposed to glucose deprivation for different time points (0, 1, 3, and 5 hr). Next, cells were centrifuged, washed with PBS, and counted using a Tali image-based cytometer (Life Technologies).

Cell Survival Assay

Cells seeded in 12-well plates in triplicate and allowed to grow to 80% confluence were treated with vehicle (positive control), 25 μM 5-FU, 5 μM CQ or 25 μM 5-FU, and 5 μM CQ. After 48 hr, the cells were washed with PBS, fixed in 4% paraformaldehyde, and stained with 0.1% crystal violet. Crystal violet was dissolved with 1 mol/l acetic acid, and absorbance at 595 nm was measured.

Wound-Healing Assay

Pml$^{+/+}$ and *Pml*$^{-/-}$ MEFs seeded in 6-well plates and grown to 90% confluence were treated with vehicle (positive control), 25 μM 5-FU, 5 μM CQ or 25 μM 5-FU, and 5 μM CQ 1 hr before wounding. The cell monolayer was wounded with a P200 pipette tip. Cells were monitored and captured by phase-contrast microscopy.

Migration Assay

In vitro cell migration assays were performed using Costar Transwell permeable polycarbonate supports (8.0-mm pores) in 24-well plates (Corning). Before seeding, the lower compartment was incubated with DMEM plus 10% FBS supplemented with vehicle (positive control), 25 μM 5-FU, 5 μM CQ or 25 μM 5-FU, and 5 μM CQ. Non-migrated cells were removed using a cotton swab, and migrated cells were fixed and stained with crystal violet.

Mouse Treatment Studies

Tumor xenografts or syngeneic tumors were obtained by subcutaneously implanting 5 × 10^6 transformed *Pml*$^{+/+}$ and *Pml*$^{-/-}$ MEFs in 50% Matrigel (BD Biosciences) in female nude mice or sv129 mice, respectively. Tumor growth was monitored daily, and tumor volumes were measured every other day.

Detection of Cell Death In Vivo

After an intravenous (i.v.) injection of 100 μl SR-FLIVO (Immunochemistry Technologies) via the lateral tail vein, the FLIVO reagent was allowed to circulate in the mouse for 30 min before sacrifice. The tumors were excised, frozen, sectioned, and stained for nuclei using DRAQ5 according to the manufacturer's protocol (Cell Signaling Technology). Images were acquired using an inverted confocal microscope.

Statistical Analysis

Unless otherwise indicated, all assays were performed independently and in triplicate, yielding comparable results. The data, which are presented as the means ± SEM, were analyzed using Microsoft Excel (Microsoft), and significance was determined by Student's t tests. ***$p < 0.005$, **$p < 0.01$, and *$p < 0.05$ were considered significant.

SUPPLEMENTAL INFORMATION

Supplemental Information includes Supplemental Experimental Procedures and six figures and can be found with this article online at http://dx.doi.org/10.1016/j.celrep.2016.07.082.

AUTHOR CONTRIBUTIONS

C.G. conceived and designed the experiments. C.G., G.K., and P.P. wrote the manuscript. S.M., M.B., S.P., and M.P. conducted the experiments. F.P. helped with mouse experiments. The immunohistochemistry (IHC) was performed by G.L., R.G., and E.M. TEM and EM analyses were performed by C.T. and A.R. The data were analyzed by S.M., M.B., S.P., C.T., G.L., P.P.P., G.K., P.P., and C.G.

ACKNOWLEDGMENTS

This study was supported mainly by the Italian Association for Cancer Research (AIRC) to C.G. (MFAG-13521). C.G. is supported also by the Italian Ministry of Health and local funds from the University of Ferrara. P.P. is grateful to Camilla degli Scrovegni for continuous support and his lab is supported by Telethon (GGP15219/B), AIRC (IG-14442), the Italian Cystic Fibrosis Research Foundation (19/2014), the Italian Ministry of Education, University and Research (COFIN no. 20129JLHSY_002, FIRB no. RBAP11FXBC_002, and Futuro in Ricerca no. RBFR10EGVP_001), local funds from the University of Ferrara and the Italian Ministry of Health. S.P. was supported by a research fellowship FISM—Fondazione Italiana Sclerosi Multipla—cod. 2014/B/3.

Received: January 8, 2016
Revised: June 3, 2016
Accepted: July 28, 2016
Published: August 18, 2016

REFERENCES

Ablain, J., Rice, K., Soilihi, H., de Reynies, A., Minucci, S., and de Thé, H. (2014). Activation of a promyelocytic leukemia-tumor protein 53 axis underlies acute promyelocytic leukemia cure. Nat. Med. *20*, 167–174.

Amaravadi, R.K., Lippincott-Schwartz, J., Yin, X.M., Weiss, W.A., Takebe, N., Timmer, W., DiPaola, R.S., Lotze, M.T., and White, E. (2011). Principles and current strategies for targeting autophagy for cancer treatment. Clin. Cancer Res. *17*, 654–666.

Baughman, J.M., Perocchi, F., Girgis, H.S., Plovanich, M., Belcher-Timme, C.A., Sancak, Y., Bao, X.R., Strittmatter, L., Goldberger, O., Bogorad, R.L., et al. (2011). Integrative genomics identifies MCU as an essential component of the mitochondrial calcium uniporter. Nature *476*, 341–345.

Bonora, M., Giorgi, C., Bononi, A., Marchi, S., Patergnani, S., Rimessi, A., Rizzuto, R., and Pinton, P. (2013). Subcellular calcium measurements in mammalian cells using jellyfish photoprotein aequorin-based probes. Nat. Protoc. *8*, 2105–2118.

Booth, L.A., Tavallai, S., Hamed, H.A., Cruickshanks, N., and Dent, P. (2014). The role of cell signalling in the crosstalk between autophagy and apoptosis. Cell. Signal. *26*, 549–555.

Boroughs, L.K., and DeBerardinis, R.J. (2015). Metabolic pathways promoting cancer cell survival and growth. Nat. Cell Biol. *17*, 351–359.

Boya, P., González-Polo, R.A., Casares, N., Perfettini, J.L., Dessen, P., Larochette, N., Métivier, D., Meley, D., Souquere, S., Yoshimori, T., et al. (2005). Inhibition of macroautophagy triggers apoptosis. Mol. Cell. Biol. *25*, 1025–1040.

Cárdenas, C., Miller, R.A., Smith, I., Bui, T., Molgó, J., Müller, M., Vais, H., Cheung, K.H., Yang, J., Parker, I., et al. (2010). Essential regulation of cell bioenergetics by constitutive InsP3 receptor Ca2+ transfer to mitochondria. Cell *142*, 270–283.

Carracedo, A., Cantley, L.C., and Pandolfi, P.P. (2013). Cancer metabolism: Fatty acid oxidation in the limelight. Nat. Rev. Cancer *13*, 227–232.

Cheng, X., Guo, S., Liu, Y., Chu, H., Hakimi, P., Berger, N.A., Hanson, R.W., and Kao, H.Y. (2013). Ablation of promyelocytic leukemia protein (PML) re-patterns energy balance and protects mice from obesity induced by a Western diet. J. Biol. Chem. *288*, 29746–29759.

Chittaranjan, S., Bortnik, S., Dragowska, W.H., Xu, J., Abeysundara, N., Leung, A., Go, N.E., DeVorkin, L., Weppler, S.A., Gelmon, K., et al. (2014). Autophagy inhibition augments the anticancer effects of epirubicin treatment in anthracycline-sensitive and -resistant triple-negative breast cancer. Clin. Cancer Res. *20*, 3159–3173.

Criollo, A., Maiuri, M.C., Tasdemir, E., Vitale, I., Fiebig, A.A., Andrews, D., Molgó, J., Díaz, J., Lavandero, S., Harper, F., et al. (2007). Regulation of autophagy by the inositol trisphosphate receptor. Cell Death Differ. *14*, 1029–1039.

De Stefani, D., Raffaello, A., Teardo, E., Szabò, I., and Rizzuto, R. (2011). A forty-kilodalton protein of the inner membrane is the mitochondrial calcium uniporter. Nature *476*, 336–340.

Degenhardt, K., Mathew, R., Beaudoin, B., Bray, K., Anderson, D., Chen, G., Mukherjee, C., Shi, Y., Gélinas, C., Fan, Y., et al. (2006). Autophagy promotes tumor cell survival and restricts necrosis, inflammation, and tumorigenesis. Cancer Cell *10*, 51–64.

Egan, D.F., Shackelford, D.B., Mihaylova, M.M., Gelino, S., Kohnz, R.A., Mair, W., Vasquez, D.S., Joshi, A., Gwinn, D.M., Taylor, R., et al. (2011). Phosphorylation of ULK1 (hATG1) by AMP-activated protein kinase connects energy sensing to mitophagy. Science *331*, 456–461.

Eisenberg-Lerner, A., Bialik, S., Simon, H.U., and Kimchi, A. (2009). Life and death partners: Apoptosis, autophagy and the cross-talk between them. Cell Death Differ. *16*, 966–975.

Esteban-Martínez, L., and Boya, P. (2015). Autophagic flux determination in vivo and ex vivo. Methods *75*, 79–86.

Galluzzi, L., Pietrocola, F., Levine, B., and Kroemer, G. (2014). Metabolic control of autophagy. Cell *159*, 1263–1276.

Giorgi, C., Ito, K., Lin, H.K., Santangelo, C., Wieckowski, M.R., Lebiedzinska, M., Bononi, A., Bonora, M., Duszynski, J., Bernardi, R., et al. (2010). PML regulates apoptosis at endoplasmic reticulum by modulating calcium release. Science *330*, 1247–1251.

Giorgi, C., Bonora, M., Missiroli, S., Poletti, F., Ramirez, F.G., Morciano, G., Morganti, C., Pandolfi, P.P., Mammano, F., and Pinton, P. (2015a). Intravital imaging reveals p53-dependent cancer cell death induced by phototherapy via calcium signaling. Oncotarget *6*, 1435–1445.

Giorgi, C., Bonora, M., Sorrentino, G., Missiroli, S., Poletti, F., Suski, J.M., Galindo Ramirez, F., Rizzuto, R., Di Virgilio, F., Zito, E., et al. (2015b). p53 at the endoplasmic reticulum regulates apoptosis in a Ca2+-dependent manner. Proc. Natl. Acad. Sci. USA *112*, 1779–1784.

Guo, A., Salomoni, P., Luo, J., Shih, A., Zhong, S., Gu, W., and Pandolfi, P.P. (2000). The function of PML in p53-dependent apoptosis. Nat. Cell Biol. *2*, 730–736.

Gurrieri, C., Capodieci, P., Bernardi, R., Scaglioni, P.P., Nafa, K., Rush, L.J., Verbel, D.A., Cordon-Cardo, C., and Pandolfi, P.P. (2004). Loss of the tumor suppressor PML in human cancers of multiple histologic origins. J. Natl. Cancer Inst. *96*, 269–279.

Hamasaki, M., Furuta, N., Matsuda, A., Nezu, A., Yamamoto, A., Fujita, N., Oomori, H., Noda, T., Haraguchi, T., Hiraoka, Y., et al. (2013). Autophagosomes form at ER-mitochondria contact sites. Nature *495*, 389–393.

Hanahan, D., and Weinberg, R.A. (2011). Hallmarks of cancer: The next generation. Cell *144*, 646–674.

Heath-Engel, H.M., Chang, N.C., and Shore, G.C. (2008). The endoplasmic reticulum in apoptosis and autophagy: Role of the BCL-2 protein family. Oncogene *27*, 6419–6433.

Ito, K., Carracedo, A., Weiss, D., Arai, F., Ala, U., Avigan, D.E., Schafer, Z.T., Evans, R.M., Suda, T., Lee, C.H., and Pandolfi, P.P. (2012). A PML–PPAR-δ pathway for fatty acid oxidation regulates hematopoietic stem cell maintenance. Nat. Med. *18*, 1350–1358.

Jouaville, L.S., Pinton, P., Bastianutto, C., Rutter, G.A., and Rizzuto, R. (1999). Regulation of mitochondrial ATP synthesis by calcium: Evidence for a long-term metabolic priming. Proc. Natl. Acad. Sci. USA *96*, 13807–13812.

Kim, J., Kundu, M., Viollet, B., and Guan, K.L. (2011). AMPK and mTOR regulate autophagy through direct phosphorylation of Ulk1. Nat. Cell Biol. *13*, 132–141.

Klionsky, D.J., Abdalla, F.C., Abeliovich, H., Abraham, R.T., Acevedo-Arozena, A., Adeli, K., Agholme, L., Agnello, M., Agostinis, P., Aguirre-Ghiso, J.A., et al. (2012). Guidelines for the use and interpretation of assays for monitoring autophagy. Autophagy *8*, 445–544.

Klionsky, D.J., Abdelmohsen, K., Abe, A., Abedin, M.J., Abeliovich, H., Acevedo Arozena, A., Adachi, H., Adams, C.M., Adams, P.D., Adeli, K., et al. (2016). Guidelines for the use and interpretation of assays for monitoring autophagy (3rd edition). Autophagy *12*, 1–222.

Lallemand-Breitenbach, V., Zhu, J., Puvion, F., Koken, M., Honoré, N., Doubeikovsky, A., Duprez, E., Pandolfi, P.P., Puvion, E., Freemont, P., and de Thé, H. (2001). Role of promyelocytic leukemia (PML) sumolation in nuclear body formation, 11S proteasome recruitment, and As2O3-induced PML or PML/retinoic acid receptor alpha degradation. J. Exp. Med. *193*, 1361–1371.

Li, J., Hou, N., Faried, A., Tsutsumi, S., and Kuwano, H. (2010). Inhibition of autophagy augments 5-fluorouracil chemotherapy in human colon cancer in vitro and in vivo model. Eur. J. Cancer *46*, 1900–1909.

Lin, T.C., Chen, Y.R., Kensicki, E., Li, A.Y., Kong, M., Li, Y., Mohney, R.P., Shen, H.M., Stiles, B., Mizushima, N., et al. (2012). Autophagy: Resetting glutamine-dependent metabolism and oxygen consumption. Autophagy *8*, 1477–1493.

Maes, H., Rubio, N., Garg, A.D., and Agostinis, P. (2013). Autophagy: Shaping the tumor microenvironment and therapeutic response. Trends Mol. Med. *19*, 428–446.

Maiuri, M.C., Zalckvar, E., Kimchi, A., and Kroemer, G. (2007). Self-eating and self-killing: Crosstalk between autophagy and apoptosis. Nat. Rev. Mol. Cell Biol. *8*, 741–752.

Mariño, G., Niso-Santano, M., Baehrecke, E.H., and Kroemer, G. (2014). Self-consumption: The interplay of autophagy and apoptosis. Nat. Rev. Mol. Cell Biol. *15*, 81–94.

Mihaylova, M.M., and Shaw, R.J. (2011). The AMPK signalling pathway coordinates cell growth, autophagy and metabolism. Nat. Cell Biol. *13*, 1016–1023.

Mizushima, N., Yoshimori, T., and Levine, B. (2010). Methods in mammalian autophagy research. Cell *140*, 313–326.

Morselli, E., Shen, S., Ruckenstuhl, C., Bauer, M.A., Mariño, G., Galluzzi, L., Criollo, A., Michaud, M., Maiuri, M.C., Chano, T., et al. (2011). p53 inhibits autophagy by interacting with the human ortholog of yeast Atg17, RB1CC1/FIP200. Cell Cycle *10*, 2763–2769.

Nazio, F., Strappazzon, F., Antonioli, M., Bielli, P., Cianfanelli, V., Bordi, M., Gretzmeier, C., Dengjel, J., Piacentini, M., Fimia, G.M., and Cecconi, F. (2013). mTOR inhibits autophagy by controlling ULK1 ubiquitylation, self-association and function through AMBRA1 and TRAF6. Nat. Cell Biol. *15*, 406–416.

Papa, A., Cordon-Cardo, C., Bernardi, R., and Pandolfi, P.P. (2012). Compound in vivo inactivation of Pml and p53 uncovers a functional interaction in angiosarcoma suppression. Genes Cancer *3*, 599–603.

Pearson, M., and Pelicci, P.G. (2001). PML interaction with p53 and its role in apoptosis and replicative senescence. Oncogene *20*, 7250–7256.

Pearson, M., Carbone, R., Sebastiani, C., Cioce, M., Fagioli, M., Saito, S., Higashimoto, Y., Appella, E., Minucci, S., Pandolfi, P.P., and Pelicci, P.G. (2000). PML regulates p53 acetylation and premature senescence induced by oncogenic Ras. Nature *406*, 207–210.

Piazza, F., Gurrieri, C., and Pandolfi, P.P. (2001). The theory of APL. Oncogene *20*, 7216–7222.

Rabinowitz, J.D., and White, E. (2010). Autophagy and metabolism. Science *330*, 1344–1348.

Ren, Y., Xie, Y., Chai, L., Wang, S., and Cheng, M. (2011). Autophagy modification augmented the treatment effects initiated by arsenic trioxide in NB4 cells. Med. Oncol. *28*, 231–236.

Rosenfeldt, M.T., Nixon, C., Liu, E., Mah, L.Y., and Ryan, K.M. (2012). Analysis of macroautophagy by immunohistochemistry. Autophagy *8*, 963–969.

Sehgal, A.R., Konig, H., Johnson, D.E., Tang, D., Amaravadi, R.K., Boyiadzis, M., and Lotze, M.T. (2015). You eat what you are: Autophagy inhibition as a therapeutic strategy in leukemia. Leukemia *29*, 517–525.

Selvakumaran, M., Amaravadi, R.K., Vasilevskaya, I.A., and O'Dwyer, P.J. (2013). Autophagy inhibition sensitizes colon cancer cells to antiangiogenic and cytotoxic therapy. Clin. Cancer Res. *19*, 2995–3007.

Strohecker, A.M., Guo, J.Y., Karsli-Uzunbas, G., Price, S.M., Chen, G.J., Mathew, R., McMahon, M., and White, E. (2013). Autophagy sustains mitochondrial glutamine metabolism and growth of BrafV600E-driven lung tumors. Cancer Discov. *3*, 1272–1285.

Su, Z., Yang, Z., Xu, Y., Chen, Y., and Yu, Q. (2015). Apoptosis, autophagy, necroptosis, and cancer metastasis. Mol. Cancer *14*, 48.

Tasdemir, E., Maiuri, M.C., Galluzzi, L., Vitale, I., Djavaheri-Mergny, M., D'Amelio, M., Criollo, A., Morselli, E., Zhu, C., Harper, F., et al. (2008). Regulation of autophagy by cytoplasmic p53. Nat. Cell Biol. *10*, 676–687.

Vance, J.E. (1990). Phospholipid synthesis in a membrane fraction associated with mitochondria. J. Biol. Chem. *265*, 7248–7256.

Wieckowski, M.R., Giorgi, C., Lebiedzinska, M., Duszynski, J., and Pinton, P. (2009). Isolation of mitochondria-associated membranes and mitochondria from animal tissues and cells. Nat. Protoc. *4*, 1582–1590.

Xu, Y., Xia, X., and Pan, H. (2013). Active autophagy in the tumor microenvironment: A novel mechanism for cancer metastasis. Oncol. Lett. *5*, 411–416.

Cell Reports, Volume *16*

Supplemental Information

PML at Mitochondria-Associated Membranes Is Critical for the Repression of Autophagy and Cancer Development

Sonia Missiroli, Massimo Bonora, Simone Patergnani, Federica Poletti, Mariasole Perrone, Roberta Gafà, Eros Magri, Andrea Raimondi, Giovanni Lanza, Carlo Tacchetti, Guido Kroemer, Pier Paolo Pandolfi, Paolo Pinton, and Carlotta Giorgi

SUPPLEMENTAL DATA ITEMS

Supplemental figures and legends

Figure S1

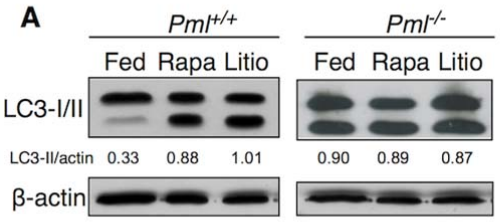

B

Quantification normalized on Sigma 1-R			
MAMs	*Pml*$^{+/+}$	*Pml*$^{-/-}$	% of increase $^{-/-}$ v $^{+/+}$
ATG14	0.11	0.25	127.27%
STX17	0.26	0.58	123.07%

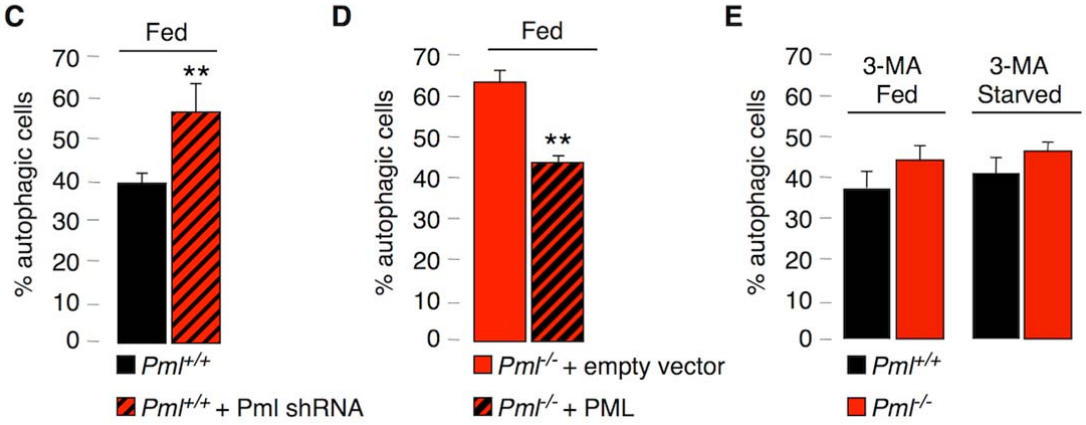

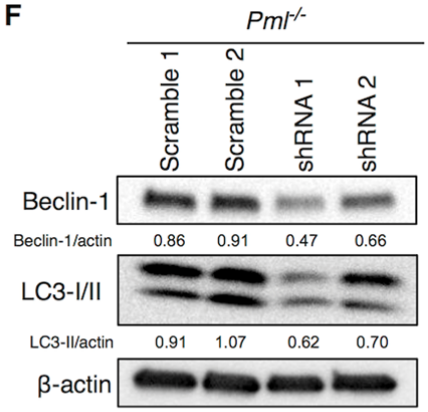

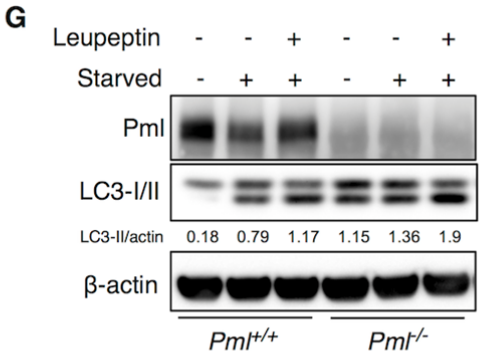

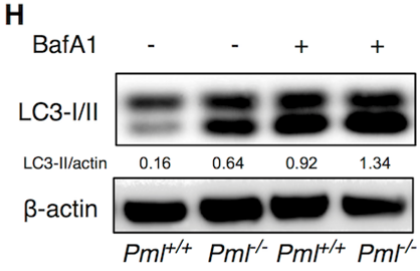

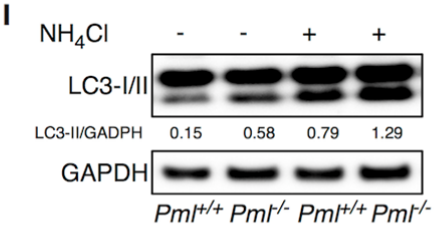

Figure S1, Related to Figure 1. High levels of autophagy under PML KO conditions, either *in vitro* or *in vivo*.
(A) Induction of LC3-I lipidation following treatment with rapamycin (100 nM, 24 h) and lithium (10 mM, 24 h) in $Pml^{+/+}$ and $Pml^{-/-}$ MEFs.
(B) ATG14 and STX17 protein quantification at MAM regions normalized to the amount of Sigma 1-R.
(C-D) Formation of GFP-LC3 puncta under (C) Pml shRNA conditions or (D) after the re-introduction of PML into $Pml^{-/-}$ MEFs. Bars: S.E.M. ** $p < 0.01$, n=3.
(E) Percentage of GFP-LC3 puncta-positive cells (MEFs) after 3-MA (10 mM, 3 h) treatment under fed and starved conditions (serum deprivation, 1 h). Bars: S.E.M.
(F) Reduced levels of autophagy in $Pml^{-/-}$ MEFs after Beclin-1 silencing.
(G) *In vivo* autophagic flux assessed by immunoblot for endogenous LC3 in $Pml^{+/+}$ and $Pml^{-/-}$ mice liver after leupeptin treatment (Esteban-Martinez and Boya, 2015).
(H) Accumulation of LC3-II obtained by interrupting the autophagosome-lysosome fusion step with bafilomycin A1 in MEF cells (Klionsky et al., 2016).
(I) LC3 turnover assay to measure the autophagic flux in MEFs cultured in the presence of ammonium chloride (NH_4Cl).

Figure S2

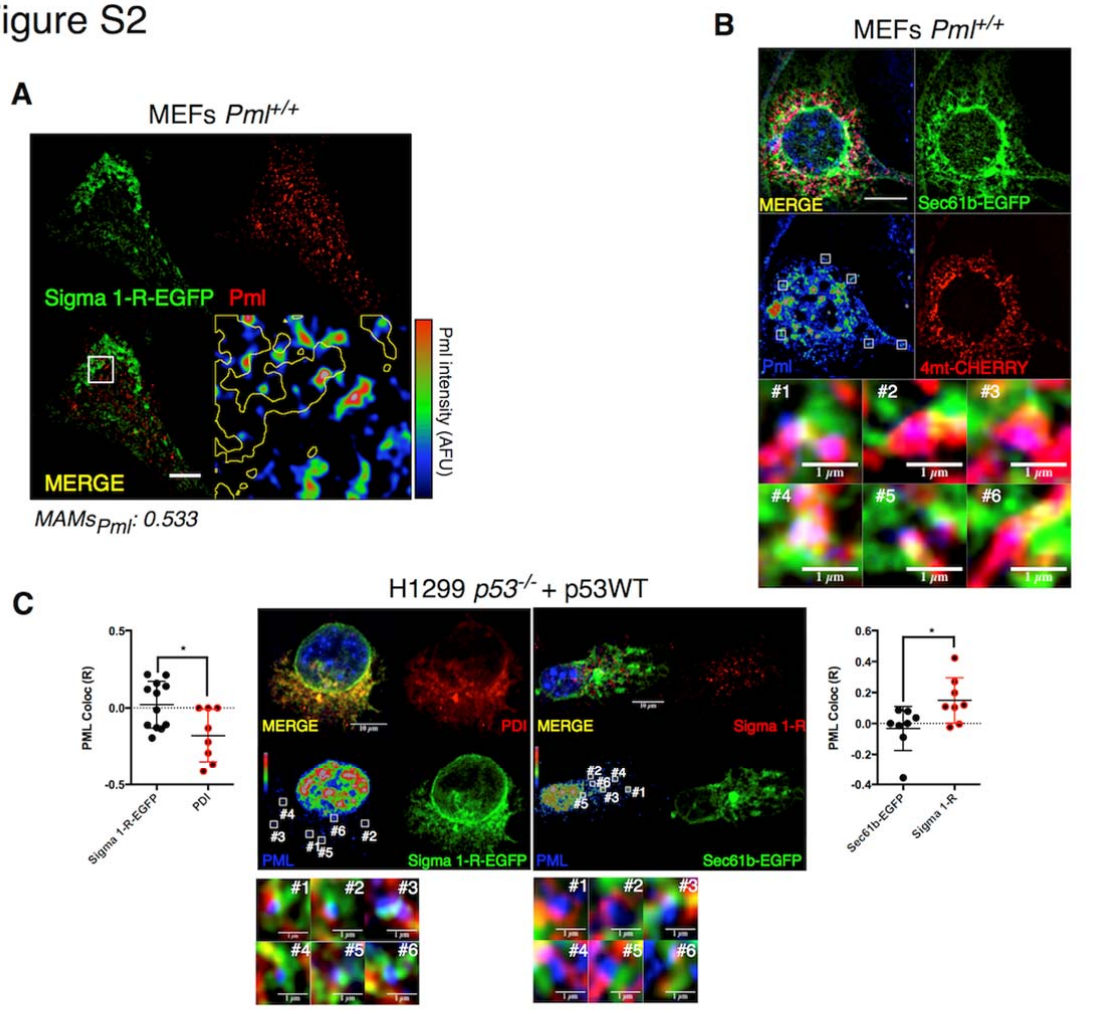
A
MEFs Pml+/+
Sigma 1-R-EGFP
Pml
MERGE
Pml intensity (AFU)
MAMsPml: 0.533
B
MEFs Pml+/+
MERGE
Sec61b-EGFP
Pml
4mt-CHERRY
#1
#2
#3
#4
#5
#6
C
H1299 p53-/- + p53WT
PML Coloc (R)
Sigma 1-R-EGFP
PDI
MERGE
PDI
PML
Sigma 1-R-EGFP
MERGE
Sigma 1-R
PML
Sec61b-EGFP
PML Coloc (R)
Sec61b-EGFP
Sigma 1-R

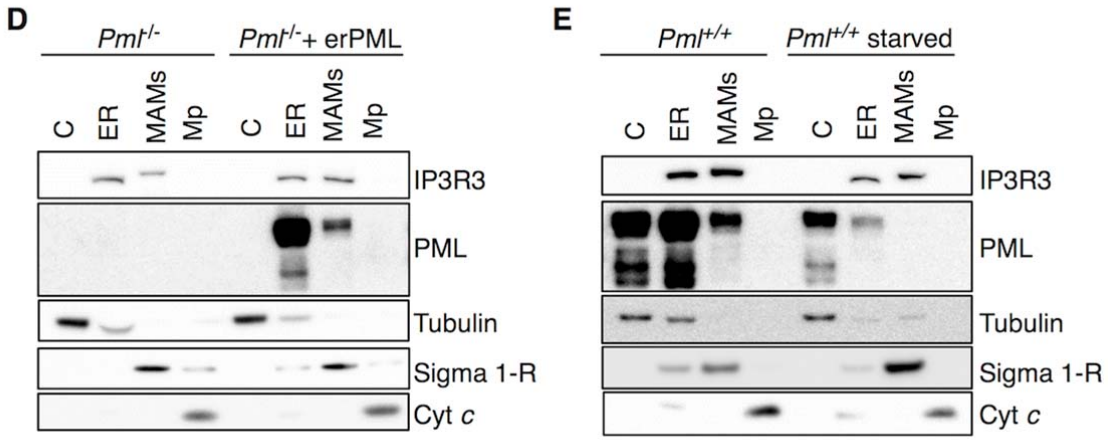
D
Pml-/-
Pml-/-+ erPML
C
ER
MAMs
Mp
IP3R3
PML
Tubulin
Sigma 1-R
Cyt c
E
Pml+/+
Pml+/+ starved
C
ER
MAMs
Mp
IP3R3
PML
Tubulin
Sigma 1-R
Cyt c

Figure S2, Related to Figure 2. Proper localization of PML at ER/MAM contact sites is fundamental to inducing autophagy.

(A) Representative confocal images of Sigma 1-R-EGFP (green) and Pml (red) in WT MEFs. The lower left panel displays the merged image of the two stains. The lower right panel displays the Pml signal overlaid with MAMs in a rainbow LUT (*$MAMs_{PML}$:* Manders coefficient for Pml staining was calculated according to Manders coefficient method as the proportion of Pml signal overlapping with the Sigma 1-R marker). Scale bar, 10 μm.

(B) Representative confocal immunofluorescence of Pml (rainbow LUT) in *$Pml^{+/+}$* MEFs expressing the mitochondrial marker 4mt-Cherry and the ER marker Sec61b-EGFP (green). Scale bar, 10 μm. On right side zoomed regions of close contacts of Pml signal together with ER and mitochondria markers (scale bar, 1 μm). Relative inset are displayed on Pml image.

(C) Representative confocal immunofluorescence of PML (rainbow LUT) and PDI (red, left panel) or Sigma 1-R (red, right panel) in H1299 cells reintroduced of $p53^{wt}$ and co-expressing Sigma 1-R-EGFP (green, left panel) or Sec61b-EGFP (green, right panel). Scale bar, 10 μm. On bottom, zoomed regions of close contacts of PML signal together with ER and MAMs markers (scale bar, 1 μm). Relative inset are displayed on PML image. Quantitative measurements of colocalization between Pml and ER or MAM marker are displayed beside each marker combination. Bars: S.E.M. * $p < 0.01$., n=3.

(D) Localization of Pml as detected *via* immunoblotting following subcellular fractionation in *$Pml^{-/-}$* MEFs transfected with erPML. C: cytosol; ER: endoplasmic reticulum; MAMs: mitochondria-associated membranes; Mp: pure mitochondria.

(E) Delocalization of Pml away from the MAM fraction in *$Pml^{+/+}$* MEF cells under starvation conditions (1 h). C: cytosol; ER: endoplasmic reticulum; MAMs: mitochondria-associated membranes; Mp: pure mitochondria.

Figure S3

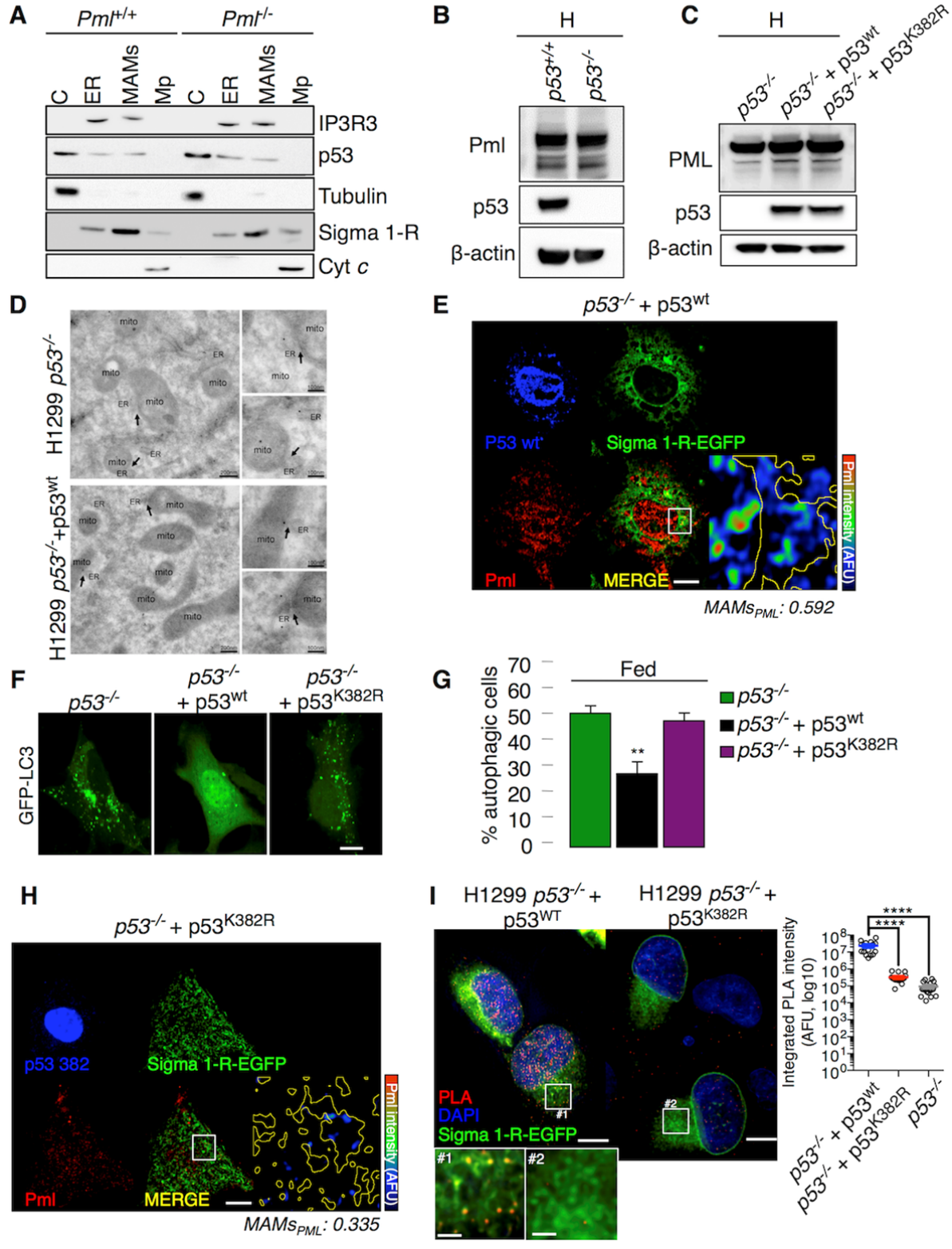
A
Pml+/+
Pml-/-
C
ER
MAMs
Mp
IP3R3
p53
Tubulin
Sigma 1-R
Cyt c
B
H
p53+/+
p53-/-
Pml
p53
β-actin
C
H
p53-/-
p53-/- + p53wt
p53-/- + p53K382R
PML
p53
β-actin
D
H1299 p53-/-
H1299 p53-/-+p53wt
mito
ER
E
p53-/- + p53wt
P53 wt
Sigma 1-R-EGFP
Pml
MERGE
Pml intensity (AFU)
MAMsPML: 0.592
F
p53-/-
p53-/- + p53wt
p53-/- + p53K382R
GFP-LC3
G
Fed
% autophagic cells
70
60
50
40
30
20
10
0
**
p53-/-
p53-/- + p53wt
p53-/- + p53K382R
H
p53-/- + p53K382R
p53 382
Sigma 1-R-EGFP
Pml
MERGE
Pml intensity (AFU)
MAMsPML: 0.335
I
H1299 p53-/- + p53WT
H1299 p53-/- + p53K382R
PLA
DAPI
Sigma 1-R-EGFP
#1
#2
Integrated PLA intensity (AFU, log10)
****
****
p53-/- + p53wt
p53-/- + p53K382R
p53-/-

Figure S3, Related to Figure 3. A p53 WT is essential for PML localization at ER/MAM contact sites and its autophagy modulation.

(A) Localization of p53 as detected via immunoblotting following subcellular fractionation in $Pml^{+/+}$ and $Pml^{-/-}$ MEFs. C: cytosol; ER: endoplasmic reticulum; MAMs: mitochondria-associated membranes; Mp: pure mitochondria. p53 immunoblot was obtained after antibodies stripping of STX17 lane from Figure 1F. Tubulin immunoblot was obtained after antibodies stripping of p53 lane from this figure.

(B) Immunoblotting of Pml levels in $p53^{+/+}$ and $p53^{-/-}$ MEFs. H: total homogenate.

(C) Immunoblotting of PML levels in $p53^{-/-}$ H1299 following the re-introduction of $p53^{wt}$ or mutant $p53^{K382R}$. H: total homogenate.

(D) Immunogold labeling of cryosections for PML. Representative images of the localization of PML in H1299 p53WT and $p53^{-/-}$ cells. Colloidal gold particles (10 nm) are associated with the ER, outer mitochondria membranes and MAMs (arrows) in p53 expressing cells. In H1299 $p53^{-/-}$ the labeling is still present on ER membranes but excluded from mitochondria or MAMs (arrows). Scale bar: left panel 1 μm, upper right panel 500 nm and lower right panel 250 nm.

(E) Immunofluorescence of Pml (red) and p53 (blue) in $p53^{-/-}$ MEFs after the re-introduction of $p53^{wt}$. Sigma 1-R-EGFP (green) was used as a MAM marker. The lower left panel displays the merged image of Pml and Sigma 1-R staining. The lower right panel displays the Pml signal overlaid with MAMs (MAM boundaries are highlighted in yellow) in a rainbow LUT ($MAMs_{PML}$: Manders coefficient for Pml staining was calculated according to Manders coefficient method as the proportion of Pml signal overlapping with the Sigma 1-R marker). Scale bar, 10 μm

(F-G) Detection of autophagy induction in $p53^{-/-}$ MEFs following the re-introduction of $p53^{wt}$ or mutant $p53^{K382R}$ based on GFP-LC3 puncta. Representative images are shown in (F) Bars: S.E.M. ** $p < 0.01$, n=4. Scale bar, 10 μm.

(H) Immunofluorescence of Pml (red) and p53 (blue) in $p53^{-/-}$ MEFs after the re-introduction of mutant $p53^{K382R}$. Sigma 1-R-EGFP (green) was used as a MAM marker. The lower left panel displays the merged image of Pml and Sigma 1-R staining. The lower right panel displays the Pml signal overlaid with MAMs (MAM boundaries are highlighted in yellow) in a rainbow LUT ($MAMs_{PML}$: Manders coefficient for Pml staining was calculated according to Manders coefficient method as the proportion of Pml signal overlapping with the Sigma 1-R marker). Scale bar, 10 μm.

(I) Representative images of PLA (red signal) from H1299 cells reintroduced of $p53^{wt}$ or $p53^{K382R}$. Sigma 1-R-EGFP (green) was used as a MAMs marker. Scale bar, 10 μm. On the bottom left panel zoomed regions display interaction sites in close contacts with Sigma 1-R-EGFP dots (scale bar, 2 μm). On upper right panel, quantitative analysis of PLA signal between PML and $p53^{wt}$ or $p53^{K382R}$. Bars: S.E.M. **** $p < 0.001$. n=3.

Figure S4

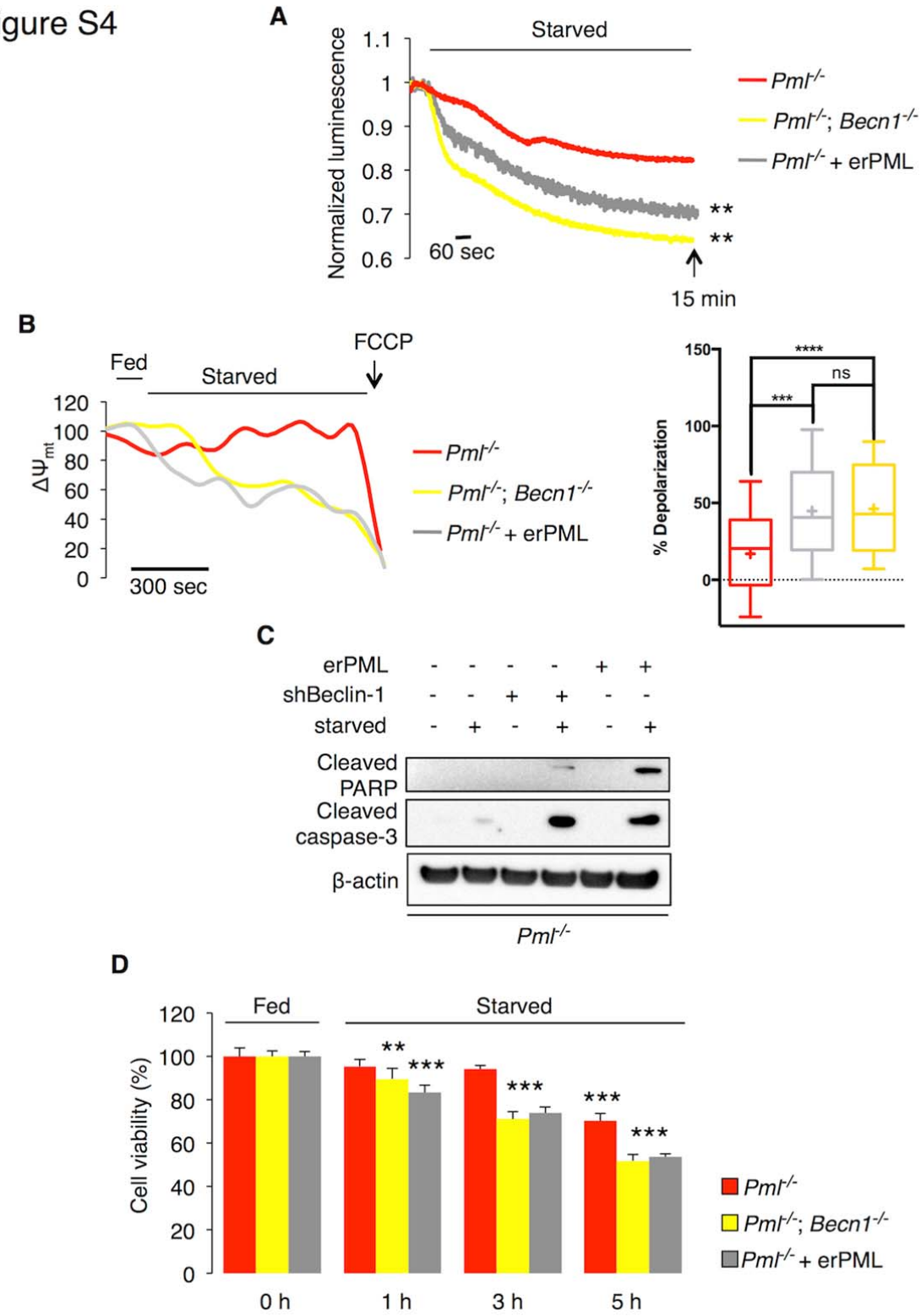
A
Starved
Normalized luminescence
1.1
1
0.9
0.8
0.7
0.6
60 sec
15 min
**
**
Pml-/-
Pml-/-; Becn1-/-
Pml-/- + erPML
B
Fed
Starved
FCCP
ΔΨmt
120
100
80
60
40
20
0
300 sec
Pml-/-
Pml-/-; Becn1-/-
Pml-/- + erPML
% Depolarization
150
100
50
0
****
ns
***
C
erPML - - - - + +
shBeclin-1 - - + + - -
starved - + - + - +
Cleaved PARP
Cleaved caspase-3
β-actin
Pml-/-
D
Fed
Starved
Cell viability (%)
120
100
80
60
40
20
0
**
***
***
***
***
0 h
1 h
3 h
5 h
Pml-/-
Pml-/-; Becn1-/-
Pml-/- + erPML

Figure S4, Related to Figure 5. Inhibition of autophagy in PML KO cells confers sensitivity to metabolic stress.
(A) Cytosolic ATP levels in MEFs *Pml*$^{-/-}$, *Pml*$^{-/-}$;*Becn1*$^{-/-}$ and *Pml*$^{-/-}$ after re-introduction of erPML chimera as measured by luciferase expression under starvation conditions (glucose deprivation for 15 min). ** $p < 0.01$, compared to KO condition, n=3.
(B) Analysis of mitochondrial membrane potential (Ψ_m) as measured by TMRM intensity in MEFs *Pml*$^{-/-}$, *Pml*$^{-/-}$; *Becn1*$^{-/-}$ and *Pml*$^{-/-}$ after re-introduction of erPML chimera. Where indicated, cells were deprived of glucose or exposed to 1 μM carbonyl cyanide p-trifluoromethoxyphenylhydrazone (FCCP). (statistical analysis cross: average, line: median, box: 25 and 75 percentile, bars: max and min value, *** $p < 0.005$, n = 3).
(C) Susceptibility to cell death and (D) cell viability of MEFs *Pml*$^{-/-}$, *Pml*$^{-/-}$; *Becn1*$^{-/-}$ and *Pml*$^{-/-}$ after re-introduction of erPML chimera under stress condition induced by glucose deprivation (3 h for western blot and the indicated hours for cell viability). Bars: S.E.M. ** $p < 0.01$, *** $p < 0.005$, n=3.

Figure S5

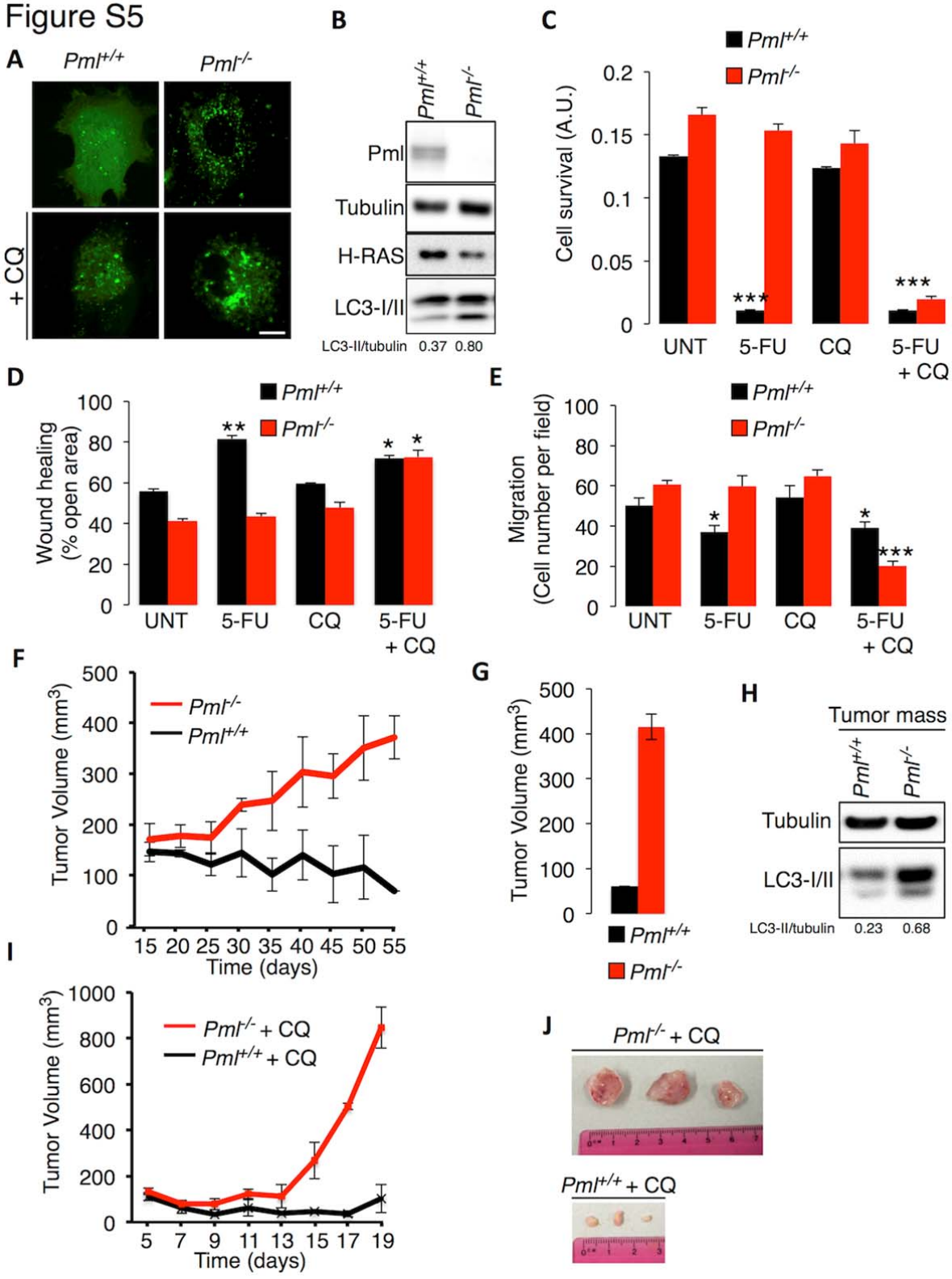
A
Pml+/+
Pml-/-
+ CQ
B
Pml+/+
Pml-/-
Pml
Tubulin
H-RAS
LC3-I/II
LC3-II/tubulin 0.37 0.80
C
Pml+/+
Pml-/-
Cell survival (A.U.)
0.2
0.15
0.1
0.05
0
***
***
UNT
5-FU
CQ
5-FU + CQ
D
Pml+/+
Pml-/-
Wound healing (% open area)
100
80
60
40
20
0
**
*
*
UNT
5-FU
CQ
5-FU + CQ
E
Pml+/+
Pml-/-
Migration (Cell number per field)
100
80
60
40
20
0
*
*
***
UNT
5-FU
CQ
5-FU + CQ
F
Pml-/-
Pml+/+
Tumor Volume (mm3)
500
400
300
200
100
0
15 20 25 30 35 40 45 50 55
Time (days)
G
Tumor Volume (mm3)
500
400
300
200
100
0
Pml+/+
Pml-/-
H
Tumor mass
Pml+/+
Pml-/-
Tubulin
LC3-I/II
LC3-II/tubulin 0.23 0.68
I
Pml-/- + CQ
Pml+/+ + CQ
Tumor Volume (mm3)
1000
800
600
400
200
0
5 7 9 11 13 15 17 19
Time (days)
J
Pml-/- + CQ
Pml+/+ + CQ

Figure S5, Related to Figure 7. Tumorigenic potential of *Pml*$^{-/-}$- and *Pml*$^{+/+}$- transformed MEFs.
(A) Representative images of LC3 puncta accumulation after CQ treatments in MEF cells. Scale bar, 10 μm.
(B) Analysis of autophagy in *Pml*$^{+/+}$ and *Pml*$^{-/-}$ transformed MEFs.
(C) Cell proliferation of *Pml*$^{+/+}$- and *Pml*$^{-/-}$-transformed MEFs as analyzed by crystal violet staining (absorbance at 595 nm) in the presence of various treatments (5-FU at 25 μM, CQ at 5 μM or 5-FU at 25 μM and CQ at 5 μM, for 24 h). Bars: S.E.M. *** $p < 0.005$ compared to untreated condition (UNT), n=3.
(D) *Pml*$^{-/-}$- transformed MEFs showed reduced wound-healing ability compared with that of *Pml*$^{+/+}$ cells (5-FU at 25 μM, CQ at 5 μM or 5-FU at 25 μM and CQ at 5 μM, 24 h). Bars: S.E.M. * $p < 0.05$, ** $p < 0.01$, compared to untreated condition (UNT), n=3.
(E) Quantification of *Pml*$^{+/+}$- and *Pml*$^{-/-}$-transformed MEF migration in the presence of various treatments (5-FU at 25 μM, CQ at 5 μM or 5-FU at 25 μM and CQ at 5 μM, 24 h). Bars: S.E.M. * $p < 0.05$, *** $p < 0.005$, compared to untreated condition (UNT), n=3.
(F) Pml+/+ sv129 mice were inoculated with Pml+/+- and Pml-/--transformed MEFs. Tumor growth was analyzed at different time points. After 55 days from inoculation tumors were excised and tumor volume (G) was measured. In parallel, the lipidation of LC3-I into the autophagic form LC3-II was assessed by immunoblot (H). Bars: S.E.M.
(I) Analysis of tumor growth following the inoculation of *Pml*$^{+/+}$- and *Pml*$^{-/-}$-transformed MEFs into nude/nude mice treated with CQ (60 mg/kg) and (J) representative images of tumors excised on day 19 after inoculation.

Figure S6

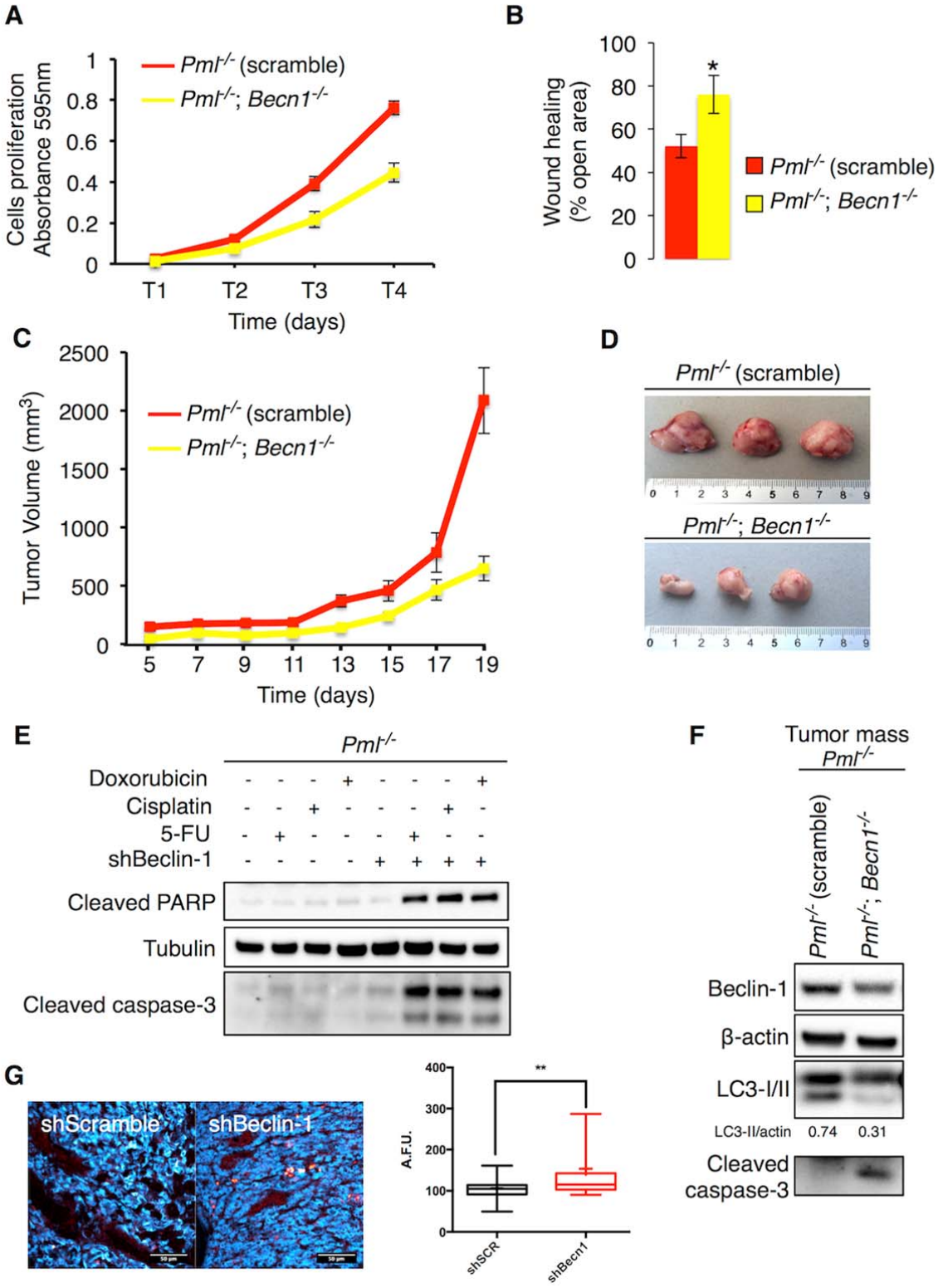
A
Cells proliferation Absorbance 595nm
Pml-/- (scramble)
Pml-/-; Becn1-/-
Time (days)
T1
T2
T3
T4
B
Wound healing (% open area)
*
Pml-/- (scramble)
Pml-/-; Becn1-/-
C
Tumor Volume (mm3)
Pml-/- (scramble)
Pml-/-; Becn1-/-
Time (days)
D
Pml-/- (scramble)
Pml-/-; Becn1-/-
E
Pml-/-
Doxorubicin
Cisplatin
5-FU
shBeclin-1
Cleaved PARP
Tubulin
Cleaved caspase-3
F
Tumor mass
Pml-/-
Pml-/- (scramble)
Pml-/-; Becn1-/-
Beclin-1
β-actin
LC3-I/II
LC3-II/actin 0.74 0.31
Cleaved caspase-3
G
shScramble
shBeclin-1
A.F.U.
**
shSCR
shBecn1

Figure S6, Related to Figure 7. Genetic inhibition of autophagy triggers apoptosis and delays tumor growth in the absence of PML.

(A) Cell proliferation of *Pml*$^{-/-}$ (scramble shRNA) and *Pml*$^{-/-}$ silenced for Beclin-1 (*Pml*$^{-/-}$; *Becn1*$^{-/-}$) MEFs as analyzed by crystal violet staining (absorbance at 595 nm).

(B) Wound-healing assay of MEFs Pml-/- (scramble shRNA) and Pml-/- silenced for Beclin-1 (Pml-/-; Becn1-/-). Bars: S.E.M. * $p < 0.05$.

(C) Tumor growth of *Pml*$^{-/-}$ (scramble shRNA) and *Pml*$^{-/-}$ silenced for Beclin-1 (*Pml*$^{-/-}$; *Becn1*$^{-/-}$) transformed MEF xenografts and respectively (D) representative images.

(E) Sensitivity to apoptosis induced by different chemotherapeutic agents (5-FU, Doxorubicin and cisplatin 10 μM, 6 h) in MEFs *Pml*$^{-/-}$ and *Pml*$^{-/-}$;*Becn1*$^{-/-}$.

(F) Analysis of autophagy and apoptosis by immunoblot of tumor tissues.

(G) Analysis of apoptosis based on the intensity of fluorescence (SR-FLIVO) emitted in tumor tissue sections, accompanied by statistical analysis. (cross: average, line: median, box: 25 and 75 percentile, bars: max and min value, *** $p < 0.005$, $n = 3$). Scale bar, 50 μm.

SUPPLEMENTAL EXPERIMENTAL PROCEDURES

Cell culture and transfection

Primary *Pml*$^{+/+}$ and *Pml*$^{-/-}$ mouse embryonic fibroblasts (MEFs) were prepared from embryos at day 13.5 of development (E13.5). Early passage (P2–P5) MEFs and H1299 cells were cultured in Dulbecco's modified Eagle's medium (DMEM) supplemented with 10% fetal bovine serum (FBS) (Life Technologies), 100 U/ml penicillin (EuroClone), 100 mg/ml streptomycin (EuroClone) and 4 mM L-glutamine (EuroClone).
Human APL NB4 cells were cultured in RPMI 1640 medium (Gibco) supplemented with 10% FBS (Gibco) and 1% penicillin-streptomycin-glutamine (100×) liquid (Gibco).
All cells were maintained at 37°C in a humidified atmosphere of 5% CO_2.
MEFs were transformed with SV40 large T antigen. MEFs were transfected with the following plasmids: PML, erPML, nuPML (Giorgi et al., 2010), p53^{WT}, p53^{K382R} (Morselli et al., 2011), MCU (De Stefani et al., 2011) and GFP-LC3 using a MicroPorator (Digital Bio). For PML depletion in WT MEFs, a specific shRNA silencing lentiviral vector (Sigma) was used. H1299 cells were transfected using a standard calcium phosphate procedure with p53^{WT} and p53^{K382R} constructs, while NB4 cells were transfected with a GFP-LC3 plasmid by electroporation.

Autophagy induction, inhibition and analysis of autophagic flux

After treatment, the cells were fixed or lysed to detect the amount of autophagosome vesicles by fluorescence microscopy (with the employment of the GFP-LC3 plasmid) or by immunoblot analysis (using LC3 antibody) (Klionsky et al., 2016; Mizushima et al., 2010).
For genetic inhibition of autophagy, we generated clones stably expressing shRNA beclin1 by culturing transfected cells in the presence of zeocin (500 μg/ml, added 48 h after transfection) for 3 weeks. Stable shRNABeclin1 clones were kept in the continuous presence of 50 μg/ml zeocin (Invitrogen).
For *in vivo* studies on the effects of starvation, mice were deprived of food for 24 h. The mice had free access to drinking water. For determination of autophagic flux *in vivo,* lysosomal activity was blocked by intraperitoneal administration of 40 mg/kg body weight of leupeptin (Sigma) in saline solution. Control animals were injected with an equivalent volume of saline solution. 4 h after injection the animals were euthanized and the livers isolated (Boya et al., 2005). After euthanasia mice tissues were processed and immunoblotted.

Quantitative analysis of GFP-LC3 dots

Pml$^{+/+}$ and *Pml*$^{-/-}$ MEFs were transfected as follows: *Pml*$^{+/+}$ and *Pml*$^{-/-}$ MEFs: 2 μg pcDNA3 + 1 μg GFP-LC3; *Pml*$^{-/-}$ MEFs expressing nuPML: 2 μg nuPML + 1 μg GFP-LC3; *Pml*$^{-/-}$ MEFs expressing erPML: 2 μg erPML + 1 μg GFP-LC3; *Pml*$^{-/-}$ MEFs expressing MCU: 2 μg MCU + 1 μg GFP-LC3.
p53$^{-/-}$ MEFs were transfected as follows: p53$^{-/-}$ MEFs: 2 μg *pcDNA3* + 1 μg GFP-LC3; p53$^{-/-}$ MEFs expressing erPML: 2 μg erPML + 1 μg GFP-LC3; p53^{WT}-overexpressing cells: 2 μg p53^{WT} + 1 μg GFP-LC3; p53^{K382R}-overexpressing cells: 2 μg p53^{K382R} + 1 μg GFP-LC3.
NB4 were transfected with 3μg GFP-LC3.

Aequorin measurements

Primary *Pml*$^{-/-}$ MEFs were transfected with the appropriate aequorin chimera targeted to the mitochondria (mtAEQmut) (Bonora et al., 2013) alone or together with MCU expression constructs as follows: *Pml*$^{-/-}$ MEFs: 0.75 μg pcDNA3 + 0.25 μg mtAEQmut; *Pml*$^{-/-}$ MEFs expressing MCU: 0.75 μg MCU + 0.25 μg mtAEQmut. All aequorin measurements were performed in Krebs-Ringer buffer (KRB) supplemented with 1 mM $CaCl_2$. An agonist was added to the same medium as specified in the figure legends. The experiments were terminated by lysing the cells with 100 μM digitonin in a hypotonic Ca^{2+}-rich solution (10 mM $CaCl_2$ in H_2O), thus discharging the remaining aequorin pool. The light signal was collected and calibrated into [Ca^{2+}] values, as described previously (Pinton et al., 2007).

Luciferase measurements

Primary *Pml*$^{+/+}$ and *Pml*$^{-/-}$ MEFs were transfected with cytosolic (untargeted) firefly luciferase (Jouaville et al., 1999). Cell luminescence was measured in the same luminometer used for the aequorin measurements with constant perfusion of KRB supplemented with 1 mM $CaCl_2$ and 20 μM luciferin for 60 sec. Then, the cells were perfused with glucose-free KRB supplemented with 1 mM $CaCl_2$ and 20 μM luciferin for 15 min. The light output of a coverslip of transfected cells was in the range of 1,000–10,000 counts per second (cps) *versus* the background at 10 cps.

Cell proliferation and viability assay, wound healing and migration assay

For the proliferation and viability assay the data are presented as a histogram showing the percentage of the cell number referred to the control condition.
For wound healing assay the cells were monitored and captured by phase-contrast microscopy (a Leica phase-contrast microscope equipped with an ICC50 HD camera and a 4X objective). Then, the percentage of the open scratched area

was measured using the Wound Healing Tool available in the software Fiji. Five replicates each of three independent experiments were performed.
For migration assay the average number of migrating cells was calculated from the total number of cells counted per chamber using the Cell Counter plugin available in the software ImageJ.

Western blot
Total cell lysates were prepared in RIPA buffer (50 mM Tris-HCl [pH 7.8], 150 mM NaCl, 1% IGEPAL CA-630, 0.5% sodium deoxycholate, 0.1% SDS, and 1 mM dithiothreitol [DTT]) supplemented with proteases and phosphatase inhibitors (2 mM Na_3VO_4, 2 mM NaF, 1 mM PMSF and protease inhibitor cocktail). In total, 20 μg protein was separated by SDS/PAGE and transferred to nitrocellulose membranes for standard western blot analysis.
The following antibodies was used: PML anti-mouse (1:1000) from Chemicon (Merck Millipore, Billerica, MA, USA); β-actin (1:3000), β-tubulin (1:3000), MCU (1:1000), p62 (1:3000), Sigma 1-R (1:1000) and STX17 (1:1000) from Sigma-Aldrich (Saint Louis, MO, USA); Atg14 (1:500) from MBL (Woburn, MA); IP3R3 (1:1000) and Cyt *c* (1:10000) from BD Biosciences (San Jose, CA, USA); ACC (1:1000), P-ACC (1:1000), AMPK (1:1000), P-AMPK (1:1000), Beclin-1 (1:1000), Caspase-3 (1:500), GAPDH (1:6000), LC3-B (1:1000), mTOR (1:1000), P-mTOR (1:1000), mouse-p53 (1:1000), p70S6 Kinase (1:1000), P-p70S6 kinase (1:1000), PARP (1:1000), ULK1 (1:1000) and P-ULK1^{Ser317} (1:1000) from Cell Signaling (Danvers, MA, USA); p53 DO-1 (1:500) and PML anti-human (1:500) from Santa Cruz (Santa Cruz, CA, USA); H-RAS antiserum (1:1000) from Novus Biologicals (Littleton, CO, USA); RARα (1:1000) from abcam (Cambridge, UK).
Isotype-matched horseradish peroxidase-conjugated secondary antibodies were used, followed by detection using chemiluminescence (PerkinElmer, Waltham, MA, USA).

Immunofluorescence assay
MEFs or H1299 were co-transfected with a plasmid coding for Sigma-1R-EGFP or SEC61b-EGFP or 4mt-Cherry and a plasmid for p53^{WT}, p53^{K382R} or PML according to experiment. Next, at 36 h after transfection, the cells were fixed in 3.7% formaldehyde in PBS for 20 min and washed three times with PBS. Formaldehyde autofluorescence was quenched by Glycine 100mM in HBSS pH 8.5 for 10 min at RT. Permeabilization of cell membranes was accomplished by 10 min incubation with 0.1% Triton X-100 in PBS, followed by a 1 h blocking with 2% bovine serum albumin (BSA) in PBS. MEFs were incubated overnight at 37°C in a wet chamber with rabbit anti-PML antibody (Abcam) and mouse anti-p53 antibody (Cell Signaling) diluted 1:100 with 2% BSA in PBS. H1299 were incubated overnight at 37°C in a wet chamber with mouse anti-PML antibody (Abcam) and rabbit anti-PDI antibody (Abcam) or rabbit anti Sigma1R (Sigma Aldrich) or mouse anti p53 (Santa Cruz) diluted 1:100 with 2% BSA in PBS. Then, staining was performed with Alexa 633 goat anti-mouse or Alexa 546 goat anti-rabbit or Alexa 488 goat anti-rabbit secondary antibodies, according to experiment. After antibody incubation, the cells were washed four times with PBS. Images were acquired using an LSM 510 laser scanning confocal microscope (Zeiss) equipped with 63X oil immersion objectives (N.A. 1.4, Zeiss) with a final pixel size of 140 nm. The pinhole size was set to allow Z sections of 1 μm thickness. Visualization of PML on MAMs was performed by overlaying the boundaries of MAM regions onto the PML signal. MAM region boundaries were obtained by thresholding the Sigma-1R-EGFP signal and converting the edges of the thresholded signal to regions of interest using the Analyze particles tool in the open source software Fiji (available at http://fiji.sc/Fiji). Then, the MAM boundaries were overlaid onto the image of the PML signal that was converted previously to a rainbow LUT. This process allowed the visualization of both weak and strong signals. All image processing was performed using the open source software Fiji. Colocalization between PML and PDI or SIGMA1R or SEC61B-EGFP or SIGMA1R-EGFP was performed using the Co-localization Threshold plugin

Measurements of mitochondrial membrane potential (Ψ_m)
Ψ_m was assessed by loading cells with 10 nM tetramethyl rhodamine methyl ester (TMRM; Life Technologies, T-668) for 35 min at 37°C in KRB supplemented with 1 mM $CaCl_2$. Images were acquired using an inverted microscope (Nikon LiveScan Swept Field Confocal Microscope Eclipse Ti equipped with NIS-Elements microscope imaging software and 40X oil immersion lens, Nikon Instruments). TMRM excitation was performed at 560 nm, and emission was collected through a 590 to 650 nm band-pass filter. After 2 min, KRB medium was exchanged with KRB without glucose. Images were acquired every 30 sec with a fixed 20 ms exposure time. FCCP (carbonyl cyanide p-trifluoromethoxyphenylhydrazone, 10 μM), an uncoupler of oxidative phosphorylation, was added after 30 acquisitions to completely collapse the electrical gradient established by the respiratory chain.
To correct TMRM signal upon oscillation induce by temperature and solution changes mitochondrial signal were normalized according to total and mitochondrial TMRM amount relationship published in (Scaduto and Grotyohann, 1999). Total and mitochondrial TMRM signal where obtained by differential thresholding before and after FCCP administration. Kinetics with stable basal value were considered correctly calibrated. Glucose deprivation induced depolarization was calculated as the reduction in TMRM signal after 20 min of glucose deprivation.

Pre-embedding immunogold electron microscopy
Cells were fixed with 4% formaldehyde in 0.1 M phosphate buffer (pH 7.4) for 1 h at room temperature. Cells were washed in PBS and treated with 50 mM glycine for 10 min. Subsequently, cells were permeabilized with 0.25%

saponin, 0.1% BSA and blocked in blocking buffer for 30 min. Cells were incubated sequentially with PML primary antibodies (Millipore MAB3738 or abcam ab72137) and goat anti-mouse or goat anti-rabbit nanogold-conjugated secondary antibodies (Nanoprobes) diluted in blocking buffer. After washes in PBS, cells were re-fixed in 1% glutaraldehyde, and nanogold was enlarged with gold enhancement solution (Nanoprobes) according to the manufacturer's instructions. Cells were post-fixed with osmium tetroxide, embedded in epon and processed into ultrathin slices. After contrasting with uranyl acetate and lead citrate, sections were analyzed with a Zeiss LEO 512 electron microscope. Images were acquired by a 2k x 2k bottom-mounted slow-scan Proscan camera controlled by EsivisionPro 3.2 software.

Migration assay

In vitro cell migration assays were performed using Costar Transwell permeable polycarbonate supports (8.0 mm pores) in 24-well plates (Corning Inc.). Before seeding (1×10^5 *Pml* $^{+/+}$ and *Pml* $^{-/-}$ MEFs), the lower compartment was incubated with DMEM plus 10% FBS supplemented with vehicle (positive control), 25 μM 5-FU, 5 μM CQ or 25 μM 5-FU and 5 μM CQ. Non-migrated cells were removed using a cotton swab, and migrated cells were fixed and stained with crystal violet. The migratory cells of five fields were imaged under a Leica phase-contrast microscope equipped with an ICC50 HD camera and a 4X objective.

Immunoelectron microscopy

H1299 *p53*$^{-/-}$ cells and H1299 after the re-introduction of p53^{wt} were fixed in 2% paraformaldehyde and 0.2% glutaraldehyde in phosphate-buffered saline (PBS), embedded in 12% gelatin and 2.3 M sucrose and frozen in liquid nitrogen. Ultrathin cryo-sections, obtained using a Reichert-Jung Ultracut E with a FC4E cryoattachment, were collected on copper-formvar-carbon-coated grids. Immunogold localization was revealed using PML antibody for endogenous human Pml (Abcam) and conjugated 10 nm protein A-gold according to published protocols (Confalonieri et al., 2000; Slot et al., 1991). All samples were examined using a Philips CM10 or a FEI Tecnai 12G2 electron microscope.

Mouse treatment studies

Procedures involving animals and their care were in conformity with institutional guidelines, and all experimental protocols were approved by the Animal Ethics Committee.

Pml$^{+/+}$ and *Pml*$^{-/-}$ sv129 mice were housed in a temperature-controlled environment with 12 h light/dark cycles and received food and water *ad libitum*.

Seven-weeks-old female athymic mice (Balb/c *nu/nu*, Harlan) were housed and handled under aseptic conditions for xenografts tumors, while seven-weeks-old female sv129 mice were used for syngeneic tumors.

Tumor volumes were measured every other day for xenograft tumors and every 5 days for syngeneic tumors with calipers using the following equation: $Volume = \pi/6 \times (a \times b^2)$, where a is the major diameter and b is the minor diameter. The athymic mice were divided into the treatment groups and the control group, with 10 mice per group. After five days, the treatments were initiated as follows: (a) PBS group, animals received intraperitoneal (i.p.) injections of 100 μl PBS every day; (b) 5-FU group, animals received i.p. injections of 30 mg/kg 5FU in 100 μl PBS twice weekly; (c) 5-FU + chloroquine (CQ) group, animals received i.p. injections of 30 mg/kg 5-FU twice weekly and 60 mg/kg CQ in 100 μl PBS every day; and (d) CQ group, animals received i.p. injections of 60 mg/kg CQ in 100 μl PBS every day. After 2 weeks of treatment, all mice were sacrificed, and tumors were immunoblotted. Sv129 mice were sacrificed after 55 days and tumors were immunoblotted.

Tissue processing

Pml$^{+/+}$ and *Pml*$^{-/-}$ mice were bred and maintained according to both the Federation for Laboratory Animal Science Associations and the Animal Experimental Ethics Committee guidelines.

For studies on the effects of starvation, mice were deprived of food for 24 h. The mice had free access to drinking water. After killing the mice, their livers were homogenized in 20 mM Tris buffer (pH 7.4) containing 150 mM NaCl, 1% Triton X-100, 10 mM EDTA and protease inhibitor cocktail. Then, tissue extracts were centrifuged at 12,000 × g at 4°C for 10 min. Finally, protein extracts (20 μg each) were subjected to SDS-PAGE and immunoblotting.

Mouse muscles were ground by mortar and pestle and lysed in a buffer containing 50 mM Tris (pH 7.5), 150 mM NaCl, 10 mM $MgCl_2$, 0.5 mM DTT, 1 mM EDTA, 10% glycerol, 2% SDS, 1% Triton X-100, Roche Complete Protease Inhibitor Cocktail, 1 mM PMSF, 1 mM $NaVO_3$, 5 mM NaF and 3 mM β-glycerophosphate. Then, tissue extracts were centrifuged at 12,000 × g at 4°C for 10 min. Finally, protein extracts (20 μg each) were subjected to SDS-PAGE and immunoblotting.

Mice tumors were excised and homogenized in lysis buffer (300 mM sucrose, 1 mM K_2HPO_4, 5.5 mM D-glucose, 20 mM Hepes, 1 mM phenylmethylsulfonylfluoride, and 0.5% IGEPAL) with a Potter pestle. Then, were centrifuged at 12,000 × g at 4°C for 15 min. Finally, protein extracts (20 μg each) were subjected to SDS-PAGE and immunoblotting.

Detection of cell death *in vivo*

After staining, the samples were mounted on coverslips and analyzed using a Zeiss LSM 510 confocal microscope equipped with an objective Fluor 40X/1.30 Oil. Images were background corrected, and signals were analyzed using open source Fiji software (available at http://fiji.sc/Fiji).

XF bioenergetic analysis

OCRs in *Pml*$^{+/+}$ and *Pml*$^{-/-}$ MEFs were measured using a Seahorse XF96 instrument (Seahorse Biosciences, North Billerica, MA) according to the manufacturer's protocols. MEFs were seeded in a XF96 microplate at a density of 15,000 cells per well and allowed to attach. The following day, the medium was exchanged, where indicated, with 175 µl unbuffered XF assay media at pH 7.4 (Seahorse Biosciences) supplemented with 5.5 mM glucose (Sigma), 1 mM sodium pyruvate and 1 mM glutamine or with 175 µl unbuffered XF assay media at pH 7.4 (Seahorse Biosciences) without glucose, sodium pyruvate or glutamine. Then, the microplate was placed in a 37°C non-CO_2 incubator for 60 min. Respiration was measured in four blocks of three for 3 min each. The first block measured the basal respiration rate. Next, 1 µm oligomycin (Seahorse Biosciences, North Billerica, MA) was added to inhibit complex V, and the second block was measured. Then, 1 µm FCCP (Seahorse Biosciences, North Billerica, MA) was added to uncouple respiration, and the third block was measured. Finally, 1 µm antimycin A (Seahorse Biosciences, North Billerica, MA) and 1 µm rotenone (Seahorse Biosciences, North Billerica, MA) were added to inhibit complex III, and the last measurements were performed. Immediately after finishing the measurements, the cells were washed with PBS, fixed in 4% paraformaldehyde and stained with 0.1% crystal violet. Crystal violet was dissolved with 1 mol/l acetic acid, and absorbance at 595 nm was measured as an index of cell amount.

Proximity Ligation Assay

p53$^{+/+}$ and *p53*$^{-/-}$ MEFs were transfected using microporator with plasmid coding for SIGMA1R-EGFP and seeded on microarray slide 16-well (thermo Fisher) at density of 20000 and 15000 respectively. Twenty-four hours after seeding cells were hybridized with antibody for PML and p53 according to the immunostaining procedure. The day after samples were hybridized with PLUS and MINUS probes blocked with goat serum 2.5% and BSA 2.5% in PBS for 30 minutes at room temperature. Proximity ligation assay was then concluded according to manufacturer instruction. PLA signal was detected by a Olympus Xcellence widefield system, and deconvolved using Fiji. After 3D digital deconvolution PLA signal was quantified as the integrated signal of each SIGMA 1-R-EGFP positive cell.

SUPPLEMENTAL REFERENCES

Bonora, M., Giorgi, C., Bononi, A., Marchi, S., Patergnani, S., Rimessi, A., Rizzuto, R., and Pinton, P. (2013). Subcellular calcium measurements in mammalian cells using jellyfish photoprotein aequorin-based probes. Nat Protoc 8, 2105-2118.

Boya, P., Gonzalez-Polo, R. A., Casares, N., Perfettini, J. L., Dessen, P., Larochette, N., Metivier, D., Meley, D., Souquere, S., Yoshimori, T., et al. (2005). Inhibition of macroautophagy triggers apoptosis. Mol Cell Biol 25, 1025-1040.

Confalonieri, S., Salcini, A. E., Puri, C., Tacchetti, C., and Di Fiore, P. P. (2000). Tyrosine phosphorylation of Eps15 is required for ligand-regulated, but not constitutive, endocytosis. J Cell Biol 150, 905-912.

De Stefani, D., Raffaello, A., Teardo, E., Szabo, I., and Rizzuto, R. (2011). A forty-kilodalton protein of the inner membrane is the mitochondrial calcium uniporter. Nature.

Esteban-Martinez, L., and Boya, P. (2015). Autophagic flux determination in vivo and ex vivo. Methods 75, 79-86.

Giorgi, C., Ito, K., Lin, H. K., Santangelo, C., Wieckowski, M. R., Lebiedzinska, M., Bononi, A., Bonora, M., Duszynski, J., Bernardi, R., et al. (2010). PML regulates apoptosis at endoplasmic reticulum by modulating calcium release. Science 330, 1247-1251.

Jouaville, L. S., Pinton, P., Bastianutto, C., Rutter, G. A., and Rizzuto, R. (1999). Regulation of mitochondrial ATP synthesis by calcium: evidence for a long-term metabolic priming. ProcNatlAcadSciUSA 96, 13807-13812.

Klionsky, D. J., Abdelmohsen, K., Abe, A., Abedin, M. J., Abeliovich, H., Acevedo Arozena, A., Adachi, H., Adams, C. M., Adams, P. D., Adeli, K., et al. (2016). Guidelines for the use and interpretation of assays for monitoring autophagy (3rd edition). Autophagy 12, 1-222.

Mizushima, N., Yoshimori, T., and Levine, B. (2010). Methods in mammalian autophagy research. Cell 140, 313-326.

Morselli, E., Shen, S., Ruckenstuhl, C., Bauer, M. A., Marino, G., Galluzzi, L., Criollo, A., Michaud, M., Maiuri, M. C., Chano, T., et al. (2011). p53 inhibits autophagy by interacting with the human ortholog of yeast Atg17, RB1CC1/FIP200. Cell Cycle 10, 2763-2769.

Pinton, P., Rimessi, A., Romagnoli, A., Prandini, A., and Rizzuto, R. (2007). Biosensors for the detection of calcium and pH. Methods Cell Biol 80, 297-325.

Scaduto, R. C., Jr., and Grotyohann, L. W. (1999). Measurement of mitochondrial membrane potential using fluorescent rhodamine derivatives. Biophys J 76, 469-477.

Slot, J. W., Geuze, H. J., Gigengack, S., Lienhard, G. E., and James, D. E. (1991). Immuno-localization of the insulin regulatable glucose transporter in brown adipose tissue of the rat. J Cell Biol 113, 123-135.